Journal of Information Systems Engineering and Management
2025, 10(4)
e-ISSN: 2468-4376
https://www.jisem-journal.com/

Research Article

Low Voltage Ride-Through of WECS Based on DFIG During a Balanced and Unbalanced Type-C Voltage Dip Using Crowbar Protection

Rayane Leulmi[1], Salima Lekhchine[2], Ammar Medoued[3], Ibtissam Bouloukza[4]
[1,3]*Department of Electrical Engineering, LES Laboratory, University of 20 August 1955, Skikda, Algeria.*
[2]*Department of Electrical Engineering, LGMM Laboratory, University of 20 August 1955-Skikda, Algeria.*
[4]*Department of Electrical Engineering, Faculty of Technology, University of 20 August 1955-Skikda, Algeria.*
Corresponding author: rayane.leulmi@univ-skikda.dz

ARTICLE INFO	**ABSTRACT**

Received: 20 March 2025
Revised: 16 May 2025
Accepted: 10 June 2025

The primary issue with variable speed wind energy conversion systems (WECS) that utilize doubly-fed induction generators (DFIG) is that partial power converters are used and the generator is directly coupled to the grid, which has a significant impact on grid disturbances like symmetrical and asymmetrical voltage dips. Voltage dips can threaten the converter on the rotor side and even damage the rotor circuit. Therefore, wind turbines must be equipped with protection mechanisms to protect the rotor converter and intermediate circuit capacitors in the event of a fault. In recent years, the crowbar protection system has been the most common configuration in generator low-voltage circuits. The objective of this work is to enhance the reactive power- supported low-voltage ride transition (LVRT) in (WECS) based on (DFIG) equipped with a parallel crowbar attached to the rotor side converter with a fuzzy logic controller (FLC) and control of the RSC and GSC negative sequence during symmetric and unbalanced type-C voltage dips. Simulations were performed in MATLAB/Simulink environment to perform a performance analysis of a 2 MW DFIG-based three-blade wind turbine with and without crowbar protection. The results have also been compared to similar research. The results demonstrated that the suggested system is robust and applicable.

Keywords: WECS, DFIG, Voltage dip, LVRT, Crowbar, Fault diagnostic, Protection system, FLC.

1.INTRODUCTION

According to statistics in recent years, the use of non-renewable energy such as nuclear power gas, natural, coal, and oil has increased due to rapid global development in various fields [1]. Therefore, if this consumption persists, we will exhaust all resources one day because we have reached our consumption limit [2]. In addition to this depletion, excessive use of this energy has negative effects on the world, for example, global warming, and maintenance costs are much higher [3]. Confronted with this world situation, researchers have found an alternative solution to replace non-renewable energies, this solution is called green energy or renewable energy [4], the latter has many advantages, including its cleanliness and naturalness, abundance, affordability, accessibility, and ability to extend the depletion curve indefinitely [5]. Green energy has been widely developed around the world. Research has proven that these energies are the only ones capable of meeting all the world's needs [6] and their use is based on the efficiency of power electronics by switching the operating mode of devices with power semiconductors.

One of these is the wind energy conversion system (WECS), the most efficient and reliable way of reducing environmental pollution and contributing to clean electricity production [7].

WECS has been increasingly popular in industrial markets in recent years, with penetration rates rising dramatically globally [8]. Investors are showing interest in these systems as one of the most promising energy sources. According to GWEC (Global Wind Energy Council) data, in 2017 and 2020 global growth increased, in 2018 exceeded 591 GW, and by 2022 will exceed 911 GW [9]. Fig 1 displays the capacity of onshore wind energy worldwide between 2013 to 2023.

Wind energy is an energy source that produces mechanical or electrical energy that can meet our growing energy needs. The most important factor of a WECS is the wind that is converted into mechanical energy through the shaft

Copyright © 2024 by Author/s and Licensed by JISEM. This is an open access article distributed under the Creative Commons Attribution License which permitsunrestricted use, distribution, and reproduction in any medium, provided the original work is properly cited.

and will turn into electricity through a machine that operates at a variable or fixed speed [10]. Today, the installation of wind systems is focused on the use of variable speed DFIG [11], these generators are the most widely used due to their many advantages [12]. Despite all the advantages, there are some disadvantages [13], among these are the DFIG stator windings' connection to the grid and the existence of static converters, which have disrupted the grid and produced the voltage dip [14]. The partial power converters used have limited power capacity and are unable to support high fault currents, resulting in rapid detachment of the generator. During voltage dip, the rotor circuit generates a high starting current, posing a risk to the rotor-side converter and potential damage to the rotor circuit. Moreover, there is a sudden change in the voltage grid magnitude [15]. Putting preventative measures in place is essential to reducing the risks and guaranteeing the system operates steadily. This phenomenon forces the stator flux to decrease abruptly and not change rapidly. It is therefore necessary to have a high voltage at the rotor, but this can be dangerous for the converter on the rotor side, which can easily deteriorate since the converter is not designed for high voltage [16]. When a malfunction occurs, WECS based on DFIG often disconnects from the system to safeguard itself. However, according to the grid codes, WECS are supposed to be connected to the grid during faults [17]. To ensure the reliability and stability of the power grid during voltage, the IEEE 1547 standard requires the connection of distributed generation resources. Therefore, it is necessary to implement specific control strategies and protection mechanisms that meet these security requirements. Failure to use any of these methods will result in reduced and degraded power converter performance and an increased probability of failure [18]. The ability of WECS to control system voltage during disturbances such as voltage dip, known as low-voltage ride-through (LVRT) or fault ride-through (FRT), is critical to ensure system reliability [19]. To ensure the robustness of the WECS control method during voltage dips, it is important to improve low-voltage ride-through by implementing effective control and protection measures to protect the system from the impact of voltage dips [20-21]. In the literature, several methods use crowbar techniques to protect DFIG rotor circuits [22]. In WECS applications, the implementation of crowbar protection mechanisms is often most commonly used to protect DFIGs and power converters from symmetrical and unbalanced voltage dips [23-24]. The importance of protecting WECS has attracted the attention of researchers. In this field, numerous recent research has been published [25-26]. Ref [27] suggests a control method with dynamic resistance and energy storage in the rotor side of the generator to increase the LVRT capacity of the planned WECS. To increase the LVRT capability of the developed WECS, a new control strategy and DC chopper were suggested in Ref.[28]. Suggested a novel control technique in Ref. [29] that makes use of machine learning to enhance WECS's LVRT performance in the event of three-phase grid failures. In Ref. [30], the DC bus voltage control method is used to perform DFIG network fault testing and protect the system from overcurrent during voltage dips. To achieve optimal response under different conditions, a gain programming technique based on artificial intelligence is used [31]. In Ref. [32], suggested a DFIG crowbar design for symmetric or asymmetric voltage dips. In Ref. [33], conducted an in-depth comparative analysis of the DFIG-based WECS extra hardware circuits and control algorithm. In Ref. [34], demonstrates the negative effects of asymmetric voltage dips, we also study the analyses of DFIG during asymmetric voltage sags. The performance of a 2 MW DFIG 3-blade wind turbine is analyzed in the MATLAB/Simulink through the study of the improvement of LVRT by crowbar protection with reactive power support for DFIG-based WECS during unbalanced type-B and type-E grid voltage dips using the negative sequence control technique, as reported in Ref. [35].

Using the crowbar protection circuit, the enhancement of the DFIG LVRT capability under symmetrical and asymmetrical voltage dips was examined in Ref. [36]. To improve the FRT capability, a fuzzy logic controller (FLC) was installed in the crowbar. MATLAB/Simulink was used to conduct the simulations. This study aims to increase the LVRT capacity of DFIG-based WECS in symmetrical and asymmetrical C-grid fault scenarios with reactive power support. Crowbar protection control is achieved by FLC and negative sequence control techniques for RSC and GSC. The performance of the proposed control scheme is investigated for a 2 MW WECS based on a DFIG. Test results have been verified in MATLAB/Simulink.The article is organized as follows: Section 2 is devoted to a detailed description of the WECS, Section 3 presents the modeling of the WECS with a simulation of a 2.4 MW wind turbine and the 2 MW DFIG on the MATLAB/Simulink platform, Section 4 is dedicated to the mathematical transformation equations essential for controlling the DFIG, RSC, and GSC of the system. Section 5 presents the detailed control of the negative sequence of the RSC and GSC and the FLC control of the crowbar protection. The negative sequence control algorithm adopted for the RSC and GSC during balanced and unbalanced type-C voltage drops is discussed in Section 6, with a comparative discussion of the results obtained with and without crowbar protection.

Copyright © 2024 by Author/s and Licensed by JISEM. This is an open access article distributed under the Creative Commons Attribution License which permitsunrestricted use, distribution, and reproduction in any medium, provided the original work is properly cited.

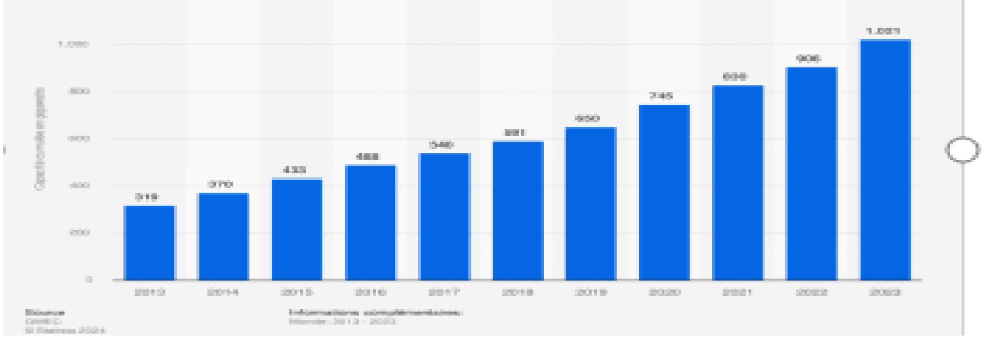

Figure 1. The global onshore wind energy capacity from 2013 to 2023

1. Wind Energy Conversion System Study

Wind energy conversion into electrical energy undergoes two crucial phases, the first being the transformation of mechanical energy through components such as the Turbine, Gearbox, and DFIG. Then, the electrical energy is converted through devices like the Back-to-Back converter, Control MPPT, and DC bus, crowbar blocks [35]. Once generated, the energy is transmitted and distributed to the grid facilitated by power converters and a transformer, along with synchronization using a phase-locked loop (PLL) [36]. The synchronization process ensures efficient power transfer between the generator rotor and the grid, contributing to the system's stability by adapting the grid's frequency and amplitude. This process guarantees a seamless and reliable transformation of wind energy into electrical energy, playing a crucial role in the current and future energy landscapes. In this study, the stator circuit of DFIG is intricately directly linked to the grid. Moreover, the rotor circuit is intricately linked to the grid through a Back-to-Back voltage source converter utilizing a passive filter to effectively mitigate higher-order harmonics [11]. Notably, one end on the generator side functions as a rectifier (RSC), while the other end of the grid serves as an inverter (GSC) incorporating a sinusoidal pulse width modulation (PWM) technique supplemented by the injection of the third harmonic. The key advantage of this remarkable topology lies in its ability to decouple the two converters, thereby facilitating separate and precise control [37]. This approach holds immense promise for enhancing grid stability and power quality.The design of the DFIG-based WECS is shown in Fig 2. However, due to the stator winding's connection to the grid and the limited capacity of the power converters, the system negatively impacts grid disturbances such as voltage dip [38].

The reduction in voltage limits the quantity of power that can be supplied to the network, resulting in an imbalance in the system's energy [39]. This common problem causes a reduction in stator torque and reactive power, and most of all, we lose control of the system. To avoid this problem, it is necessary to limit rotor currents to specific values [25]. This is done by increasing the rotor voltage amplitude to match the stator voltage. However, the RSC then reaches its maximum capacity, which is problematic as converters are only designed to generate 1/3 of the stator voltage [40]. As a result, the system can lose control during a dip, resulting in rotor overcurrents and preventing rapid stator flow. In addition, this triggers overvoltages in the DC link, which can ultimately cause grid separation [42]. Due to the voltage limitation, WECS integrates a protection device that protects them against overcurrents and overvoltages [20]. To avoid damage to the RSC in the case of an abnormal situation, a crowbar must be installed between the terminals of the rotor [32]. When there is a dip in voltage, the crowbar protection system is triggered when the rotor current exceeds the maximum limit and the DC link voltage exceeds the maximum limit. This causes the rotor current to be redirected to the crowbar protection and the RSC to be deactivated after the flux has decreased, and when the converter voltage becomes manageable for the machine, the crowbar is disconnected and the rotor converter is reactivated [36].

Copyright © 2024 by Author/s and Licensed by JISEM. This is an open access article distributed under the Creative Commons Attribution License which permitsunrestricted use, distribution, and reproduction in any medium, provided the original work is properly cited.

Journal of Information Systems Engineering and Management
2025, 10(4)
e-ISSN: 2468-4376
https://www.jisem-journal.com/

Research Article

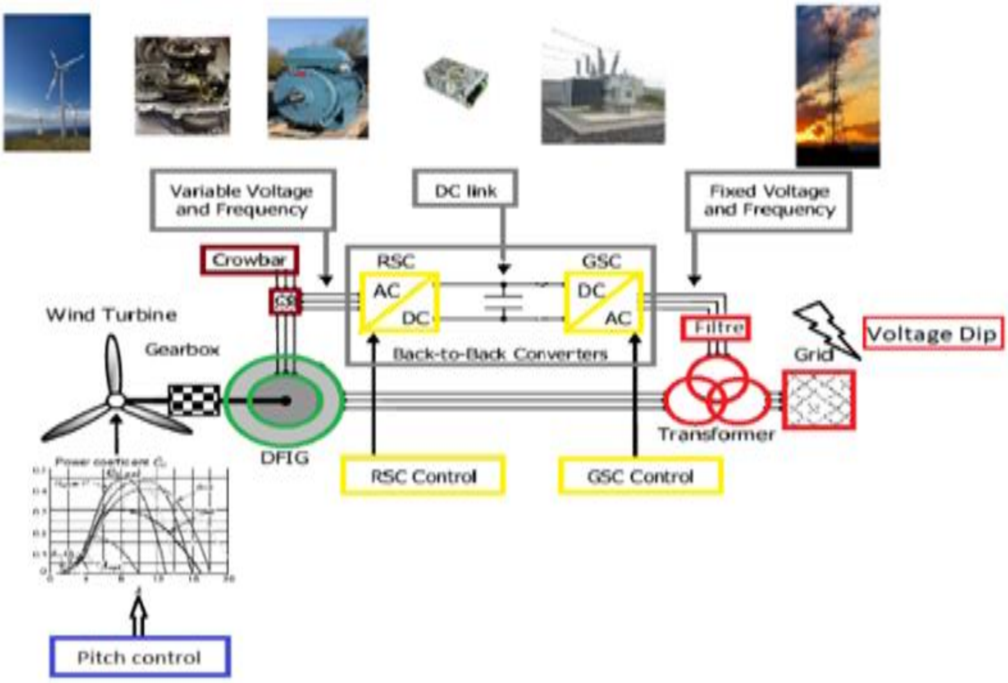

Figure 2. System configuration of the DFIG-based wind turbine

As seen in Fig 3 the rotor circuit in this study is made up of a rectifier, a controlled switch, and a resistor positioned at each rotor terminal. The crowbar is linked in parallel with this circuit. As a result, the stator flux voltage reaches a new steady state.

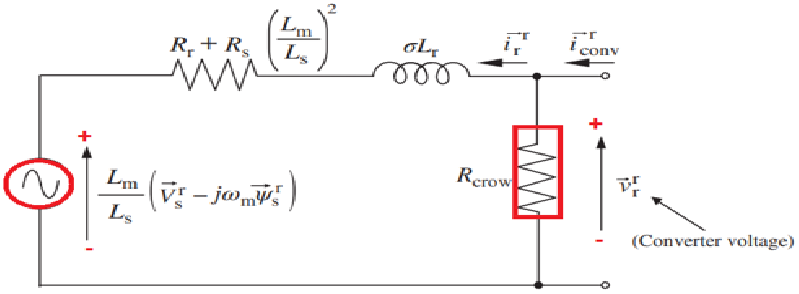

Figure 3. Equivalent circuit of DFIG with crowbar protection

2. Modeling Wind Conversion System

The RSC regulates the power generated by the DFIG and its electromagnetic torque, whereas the GSC regulates the DC bus voltage. The rotor windings and RSC are shielded from overvoltage and overcurrent using the Crowbar block. Using real DFIG parameters, the designed WECS has been extended with the asynchronous machine model from the Matlab library.

The WECS modeling based on the variable speed DFIG is simulated on MATLAB/Simulink. In Fig 4, the simulation diagram is displayed. The operation of WECS requires the mathematical development of each component in the chain. Therefore, WECS can be modeled by two main parts, modeled separately.

Copyright © 2024 by Author/s and Licensed by JISEM. This is an open access article distributed under the Creative Commons Attribution License which permitsunrestricted use, distribution, and reproduction in any medium, provided the original work is properly cited.

Journal of Information Systems Engineering and Management
2025, 10(4)
e-ISSN: 2468-4376
https://www.jisem-journal.com/
Research Article

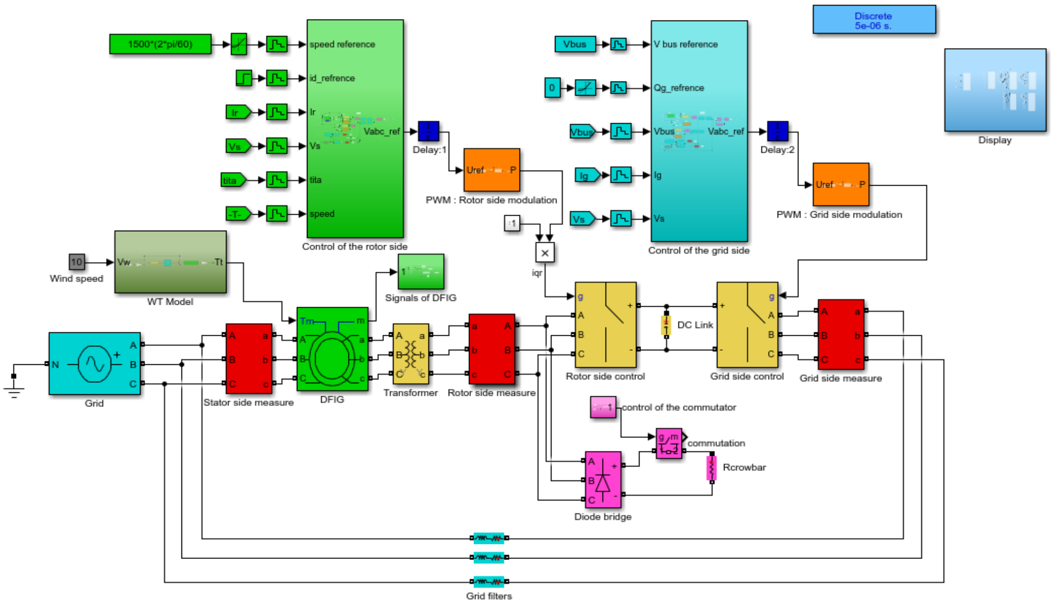

Figure 4. Diagram of (WECS) with (DFIG) for studying voltage dip using MATLAB/Simulink

3.1 Modeling of mechanical part

The mathematical model of the wind turbine is modeled by Eqs. (1)-(2) [35]:

$$p_w = \frac{1}{2}\rho\pi R^2 {V_w}^3 \quad (1)$$

$$P_{aer} = \frac{1}{2}C_p(\lambda,\beta)\rho\pi R^2 {V_w}^3 \quad (2)$$

With,

p_w: Power of the wind (w); ρ: Air density (kg/m3);R: Radius of wind generator (m);V_w: Wind speed ratio (m/s);P_{aer}: Aerodynamic power (w);C_p: The coefficients of power; T_{aer}: Aerodynamic torque (N.m);

Fig 5 illustrates the simulated evolution of the wind turbine power curve with wind speed.

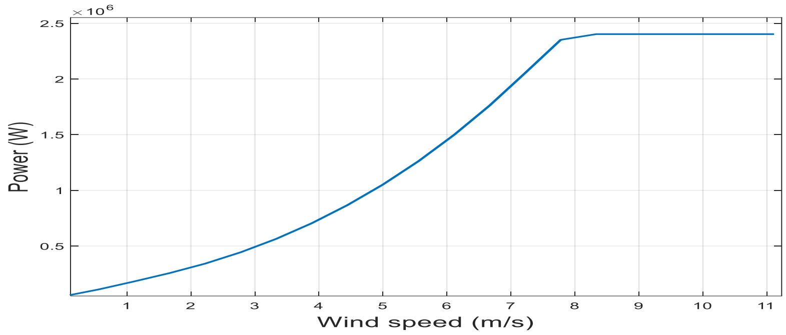

Figure 5. Power curve of the wind turbine

The tip speed ratio (TSR) is determined by the Eq. (3) [30]:

$$\lambda = \frac{\Omega_t R}{V_w} \quad (3)$$

The aerodynamic power coefficient is presented in Eq. (4)-(5) [30]:

Copyright © 2024 by Author/s and Licensed by JISEM. This is an open access article distributed under the Creative Commons Attribution License which permitsunrestricted use, distribution, and reproduction in any medium, provided the original work is properly cited.

$$C_p = k_1\left(\frac{k_2}{\lambda_i} - k_3\beta - k_4\beta^{k_5} - k_6\right)\left(e^{-k_7/\lambda_i}\right) \quad (4)$$

$$\lambda_i = \frac{1}{\lambda + k_8} - \frac{k_9}{\beta+1} \quad (5)$$

k_1	k_2	k_3	k_4	k_5	k_6	k_7	k_8	k_9
0.73	151	0.58	0.002	2.4	13.2	18.4	0.02	0.003

The aerodynamic power coefficient as a function of TSR was simulated, as shown in Fig 6.

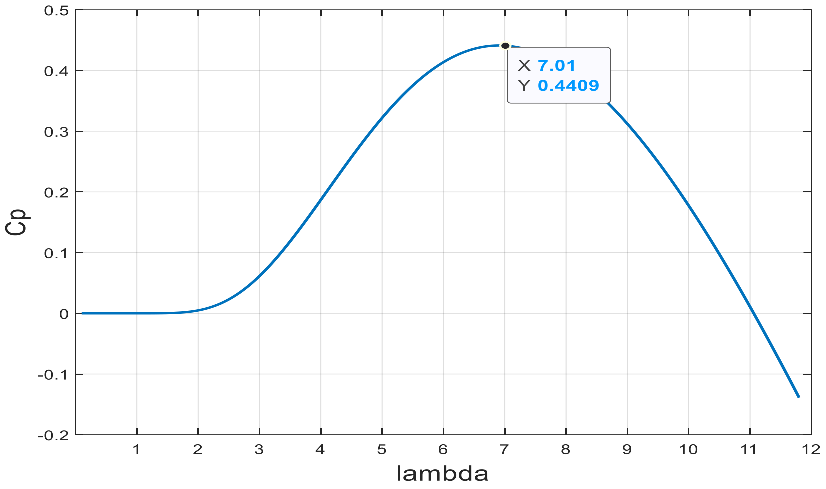

Figure 6. Power coefficient in relation to the ratio of tip speeds

The aerodynamic torque coefficient depends on the TSR and the power coefficient, as shown in Eq. (6): $C_t(\lambda) = \frac{C_p(\lambda)}{\lambda}$ (6)

The aerodynamic torque coefficient as a function of TSR was simulated, as shown in Fig 7.

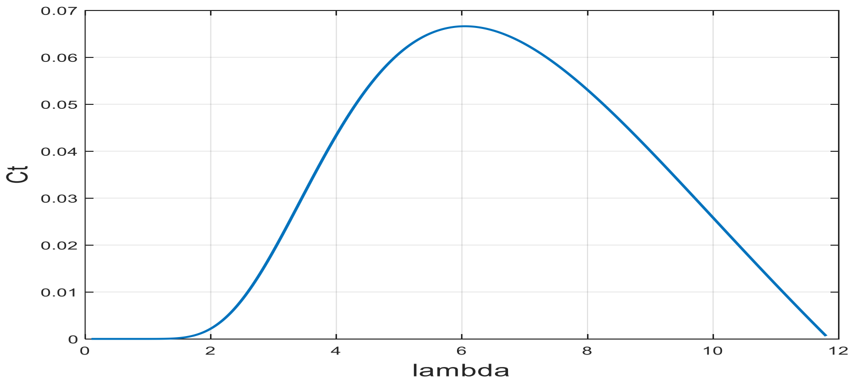

Figure 7. Coefficient torque in relation to tip speed ratio

Table 1 displays the parameters of the turbine.

Copyright © 2024 by Author/s and Licensed by JISEM. This is an open access article distributed under the Creative Commons Attribution License which permitsunrestricted use, distribution, and reproduction in any medium, provided the original work is properly cited.

Table 1. Turbine parameters

Parameter	**Value**	**Unit**
Air density	1.225	kg/m3
Tip speed ratio	7.01	/
Power coefficient	0.44	/
Radius of turbine	42	m
Pitch angle	0°	degree
Gear ratio	100	/
wind speed	10	m/s

The aerodynamic torque is given by the Eq. (7) [16]:

$$T_{aer} = \frac{P_t}{\Omega_t} = \frac{\rho\pi R^3 V_w^2}{2\lambda} C_p = \frac{1}{2}\rho\pi R^3 V_w^2 C_t \tag{7}$$

T_{aer}: Aerodynamic torque (N.m); C_t: The coefficient of torque; λ: Relative speed ratio; Ω_t: Turbine shaft speed (rpm);

The gearbox is modeled by the Eqs. (8)-(9) [37]:

$$\Omega_m = G\ \Omega_t \tag{8}$$

$$T_{load} = \frac{1}{G}\ T_{aer} \tag{9}$$

With, Ω_m: Generator speed;G: Gearbox gain;Ω_t: Turbine speed; T_{load}: The load torque applied on the generator shaft (N.m);

The simplified dynamic equation of the shaft turbine is given by the Eq. (10) [28]:

$$J\ \frac{d\Omega_m}{dt} = T_{em} - T_{load} \tag{10}$$

J: Moment of inertia (kg.m^2); T_{em}: Electromagnetic torque (N.m).

The total inertia J is presented as Eq.(11) [37]:

$$J = \frac{J_{tur}}{G} + J_m \tag{11}$$

J_{tur}: The inertia of the turbine; J_m:The inertia of the generator.

3.2 Modeling of the electrical part

3.2.1 Model of DFIG

The modeling of the stator and rotor voltages, flux, and active/reactive powers of (DFIG) can be represented in the dq frame as shown in Eq. (12)_(17) [37]:

$$\text{Stator Voltages: } \begin{cases} V_{ds} = R_s.i_{ds} + \frac{d\phi_{ds}}{dt} - \omega_s.\phi_{qs} \\ V_{qs} = R_s.i_{qs} + \frac{d\phi_{qs}}{dt} + \omega_s.\phi_{ds} \end{cases} \tag{12}$$

$$\text{Stator Flux: } \begin{cases} \Phi_{ds} = \Phi_s = L_s.i_{ds} + M.i_{qr} \\ \Phi_{qs} = L_s.i_{qs} + M.i_{dr} \end{cases} \tag{13}$$

$$\text{Stator Powers: } \begin{cases} P_s = \frac{3}{2}(V_{ds}.i_{ds} + V_{qs}.i_{qs}) \\ Q_s = \frac{3}{2}(V_{qs}.i_{ds} - V_{ds}.i_{qs}) \end{cases} \tag{14}$$

Copyright © 2024 by Author/s and Licensed by JISEM. This is an open access article distributed under the Creative Commons Attribution License which permitsunrestricted use, distribution, and reproduction in any medium, provided the original work is properly cited.

Rotor Voltages: $$\begin{cases} V_{dr} = R_r . i_{dr} + \frac{d\phi_{dr}}{dt} - \omega_r . \phi_{qr} \\ V_{qr} = R_r . i_{qr} + \frac{d\phi_{qr}}{dt} + \omega_r . \phi_{dr} \end{cases} \quad (15)$$

Rotor Flux: $$\begin{cases} \Phi_{dr} = L_r . i_{dr} + M . i_{ds} \\ \Phi_{qr} = L_r . i_{qr} + M . i_{qs} \end{cases} \quad (16)$$

Rotor Powers: $$\begin{cases} P_r = \frac{3}{2}(V_{dr} . i_{dr} + V_{qr} . i_{qr}) \\ Q_r = \frac{3}{2}(V_{qr} . i_{dr} - V_{dr} . i_{qr}) \end{cases} \quad (17)$$

Where, i_{ds} , i_{qs}, i_{dr} , i_{qr}: Stator and rotor current; R_s, R_r: Stator and rotor resistance; L_s, L_r: Stator and rotor proper inductance; M: The mutual inductance between rotor bars and stator winding;

$\omega_s \omega_r$: Stator and roto speed; P_s, P_r Stator and rotor active power (w); $Q_s Q_r$: Stator and rotor reactive power (var).

The foregoing equation allows for the simplification of the equivalent steady-state circuit of the DFIG in the dq reference frame, as illustrated in Fig 8.

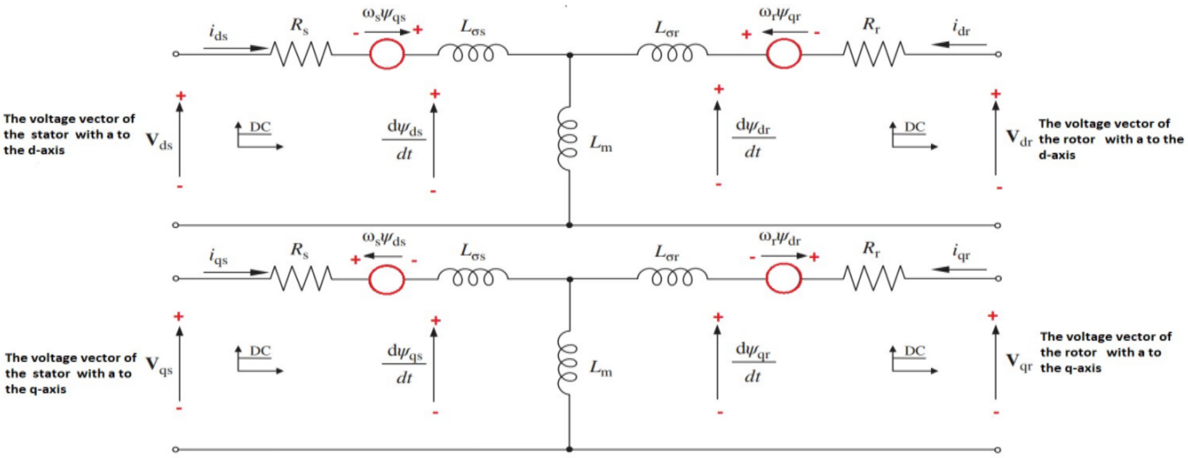

Figure 8. The DFIG equivalent circuit model in the dq frame of reference

The torque represented by Eq. (18) [37]:

$$\begin{cases} T_{em} = \frac{3}{2} \frac{PM}{L_s}(i_{dr} Ø_{qs} - i_{qr} Ø_{ds}) \\ \quad T_{em} = -\frac{3}{2} \frac{PM}{L_s} i_{qr} Ø_{ds} \end{cases} \quad (18)$$

P: The number of poles of the pair.

3.2.2 Model of back-to-back converter

Typically, back-to-back converters are modeled using a detailed model that uses switching devices in the simulation and is controlled by signals S_{a_r} , S_{b_r} , S_{c_r} , S_{a_g} , S_{b_g} , S_{c_g}. It has been proposed that back-to-back converter models allow adaptable simulations for different conditions and are used to synchronize the rotor voltage frequency with that of the stator circuit and thus with the grid [40]. In this study, two converters can be used in inverter or rectifier mode and are equipped with three switching elements and six IGBT electronic switches [37]. These switches can be operated in switching mode and connected back-to-back via diodes, either on the rotor or grid side, as shown in the figure. The DC bus is bidirectional and allows reversibility. The converter's control approach is predicated on pulse width modulation (PWM) technology, which minimizes harmonics by reducing the content of low-frequency harmonics [40].

The back-to-back design of the power converters is shown in Fig 9.

Copyright © 2024 by Author/s and Licensed by JISEM. This is an open access article distributed under the Creative Commons Attribution License which permitsunrestricted use, distribution, and reproduction in any medium, provided the original work is properly cited.

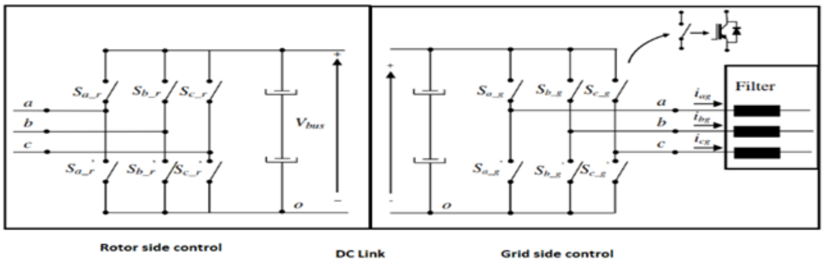

Figure. 9 Back-to-back structure of power converters

Simple voltages in matrix form are given by Eq. (19):

$$\begin{bmatrix} V_a \\ V_b \\ V_c \end{bmatrix} = \frac{1}{3}\begin{bmatrix} 2 & -1 & -1 \\ -1 & 2 & -1 \\ -1 & -1 & 2 \end{bmatrix}\begin{bmatrix} V_{ao} \\ V_{bo} \\ V_{co} \end{bmatrix} \qquad (19)$$

Moreover, the converter is modeled by Eq. (20):

$$\begin{bmatrix} V_a \\ V_b \\ V_c \end{bmatrix} = \frac{1}{3}\begin{bmatrix} 2 & -1 & -1 \\ -1 & 2 & -1 \\ -1 & -1 & 2 \end{bmatrix}\begin{bmatrix} S_{a\_r} \\ S_{b\_r} \\ S_{c\_r} \end{bmatrix} \qquad (20)$$

Eq. (21) explicitly defines the voltage between the DC bus's neutral point (n) and negative point (o):

$$\begin{bmatrix} V_{an} \\ V_{bn} \\ V_{cn} \end{bmatrix} = \frac{V_{bus}}{3}\begin{bmatrix} 2 & -1 & -1 \\ 2 & -1 & -1 \\ 2 & -1 & -1 \end{bmatrix}\begin{bmatrix} S_{a\_g} \\ S_{b\_g} \\ S_{c\_g} \end{bmatrix} \qquad (21)$$

3.2.3 *model of DC bus circuit*

The DC bus circuit model consists of a capacitor connected in parallel with a high resistor. The DC bus voltage is represented by Eqs. (22)-(23) and the DC bus circuit is shown in Fig 10. [40]:

$$V_{bus} = \int \frac{1}{C_{bus}}\, i_c\, d_t \qquad (22)$$

$$i_{res} = \frac{V_{bus}}{R_{bus}} \qquad (23)$$

With, C_{bus}: Capacity value.

The capacitor current is expressed by Eq. (24):

$$i_c = i_{r_{dc}} - i_{g_{dc}} - i_{res} \qquad (24)$$

$i_{r_{dc}}$: current through the resistance (A); $i_{g_{dc}}$: DC current flowing from the DC link to the grid (A); i_{res}: DC current flowing from the rotor to the DC link (A).

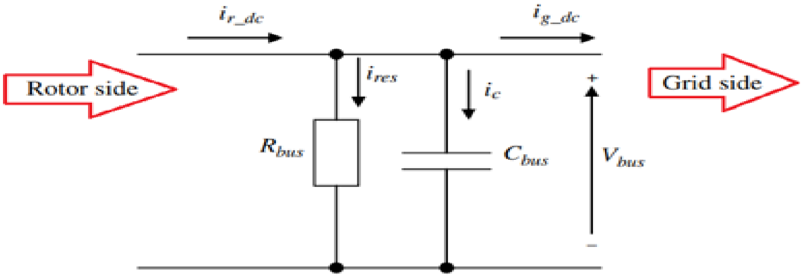

Figure. 10 DC link circuit

Copyright © 2024 by Author/s and Licensed by JISEM. This is an open access article distributed under the Creative Commons Attribution License which permitsunrestricted use, distribution, and reproduction in any medium, provided the original work is properly cited.

Journal of Information Systems Engineering and Management
2025, 10(4)
e-ISSN: 2468-4376
https://www.jisem-journal.com/

Research Article

3.2.4 model of the passive filter

The simplified model of the filter and grid is shown in Fig 11, while the voltage through the filter can be represented by Eq. (25) [36]:

$$\begin{cases} V_{af} = R_f . i_{ag} + L_f . \frac{di_{ag}}{dt} + V_{ag} \\ V_{bf} = R_f . i_{bg} + L_f . \frac{di_{bg}}{dt} + V_{bg} \\ V_{cf} = R_f . i_{cg} + L_f . \frac{di_{cg}}{dt} + V_{cg} \end{cases} \tag{25}$$

Using Park's transformation to the synchronous reference, the Eq. (25) is transformed into Eq. (26):

$$\begin{cases} V_{df} = R_f . i_{dg} + \mathrm{L}_f \frac{di_{dg}}{dt} - \omega_g \mathrm{L}_f i_{qg} + \mathrm{V}_{dg} \\ V_{qf} = R_f . i_{qg} + \mathrm{L}_f \frac{di_{qg}}{dt} + \omega_g \mathrm{L}_f i_{dg} + \mathrm{V}_{qg} \end{cases} \tag{26}$$

Where, V_{af} , V_{bf}, V_{cf} : The output voltages of the converter (V); V_{ag}, V_{bg}, V_{cg} : The grid voltages (V); ω_g : The angular speed of the grid (rad/s); R_f, L_f: The resistance and inductance of the filter;

i_{ag}, i_{bg}, i_{cg} : The currents of the grid side converter's (A); V_{df}, V_{qf}: The voltages modulated by the converter; V_{gd}, V_{gq}: The network voltages; i_{gd}, i_{gq}: The direct and quadratic components of the filter currents;

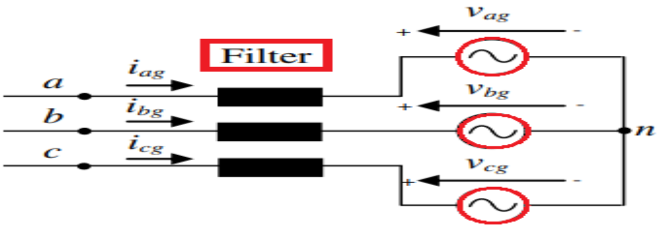

Figure 11. Simplified filter and grid model

3.2.5 Choice of crowbar resistance

This work consists of connecting a crowbar in parallel with the rotor circuit to protect it it against a voltage dip using FLC. The circuit for protection consists of rectifiers, controlled switches, and resistors placed at each rotor terminal, as shown in Fig 12.

Fault detection is guaranteed by two conditions using Eqs. (27)-(28) [35]:

1- The fault current must be less than the safety current, which is indicated by $I_r > I_{r\_limite}$.

2- The V_{bus}capacitance determines the limit of the crowbar resistance, which is indicated by $V_{bus} > V_{bus\_limite}$.

So, we can say that the size of the crowbar resistance is related to I_r and V_{bus} . In order to improve the LVRT capability of DFIG and better protect the RSC, the crowbar resistance needs to be adjusted to limit the fault current, and we take the error as the FLC input value [36].

$$\begin{cases} \frac{|\overrightarrow{V_s}(t_0)|}{\sqrt{(\omega_a L_l)^2 + (R_{cb})^2}} < I_{r,safe} \\ R_{cb,min} = \sqrt{(|\overrightarrow{V_s}(t_0)|)^2 - (\omega_a L_l I_{r,safe})^2} \ / I_{r,safe} \end{cases} \tag{27}$$

$$\begin{cases} \sqrt{3} R_{cb} \, I_{fault} < V_{DC,max} \\ R_{cb,max} = (\omega_a L_l V_{DC,max}) / \sqrt{3(|\overrightarrow{V_s}(t_0)|)^2 - (V_{DC,max})^2} \end{cases} \tag{28}$$

Where, $\overrightarrow{V_s}$: The stator voltage vector; $I_{r,safe}$: The rotor safe current; $V_{DC,max}$: The maximum acceptable voltage at the DC link; R_{cb}: The crowbar resistance; $L_l = L_{ls} + L_{lr}$; $L_s = M + L_{ls}$;

Copyright © 2024 by Author/s and Licensed by JISEM. This is an open access article distributed under the Creative Commons Attribution License which permitsunrestricted use, distribution, and reproduction in any medium, provided the original work is properly cited.

$L_r = M + L_{lr}$; L_{ls}: The leakage inductance of the stator; L_{lr}: The leakage inductance of the rotor; L_s: The inductance of the stator; L_r : The inductance of the rotor.

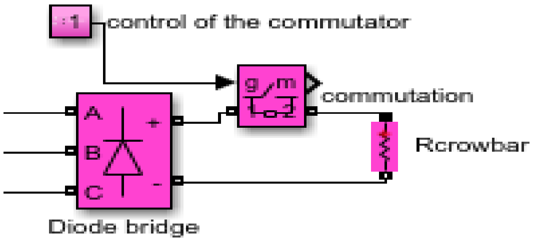

Figure 12. The crowbar protection resistance diagram

3. Control of WECS Based on DFIG For Voltage Dips

This section presents the detailed DFIG-based control of WECS during a voltage dip. The control requires the use of the conversion equations mentioned in the previous section.

The DFIG presents a complex interaction and oscillatory dynamic response due to the variable angle between the stator and rotor rotating fields under loads other than 90° [41]. To solve this problem and achieve decoupling, there are numerous control methods for RSC and GSC, which involve transforming the machine electrical variables into a reference frame that rotates with the flux vector. Flux vector control is a promising solution for improving the performance of variable-speed applications with DFIG [41]. By orienting the rotor and stator flux, indirect vector control (VCM) and direct torque control are employed. For torque control, the flux amplitude and angle are computed. The positive and negative sequence vector control with balanced rotor current technique illustrated in the figure for the RSC and GSC is based on the principle of dq axis transformation.

5.1 Control of a Variable Speed Wind Turbine

The MPPT method is widely used in the literature to control part-load wind turbines by following the path of maximum power extraction [42]. There are two different types of controllers, and in this study, we used an indirect speed controller as shown in Fig 13.

During MPPT operation, expressions are defined by Eq. (29):

$$\begin{cases} C_p = C_{p\_max} \\ \lambda = \lambda_{opt} \\ \beta = \beta_{opt} \end{cases} \tag{29}$$

The aerodynamic torque is given by the Eqs. (30) -(31) -(32):

$$T_{aer} = \frac{1}{2}\rho\pi R^3 \frac{R^2\Omega_t^2}{\lambda_{opt}^2}\frac{C_{p\_max}}{\lambda_{opt}} \tag{30}$$

Where,

$$k_{opt} = \frac{1}{2}\rho\pi\frac{R^5}{\lambda_{opt}^3 N^3}C_{p\_max} \tag{31}$$

That is, $T_{aer} = k_{opt}\Omega_t^2$ (32)

The electromagnetic torque is given by the Eq. (33):

$$T_{em} = -\frac{T_{aer}}{G} + D\,\Omega_m \tag{33}$$

Substituting Eq. (31) into Eq. (32), we obtain the electromagnetic torque as in Eq. (34):

$$T_{em} = -k_{opt}\Omega_m^2 + D\Omega_m \tag{34}$$

Copyright © 2024 by Author/s and Licensed by JISEM. This is an open access article distributed under the Creative Commons Attribution License which permitsunrestricted use, distribution, and reproduction in any medium, provided the original work is properly cited.

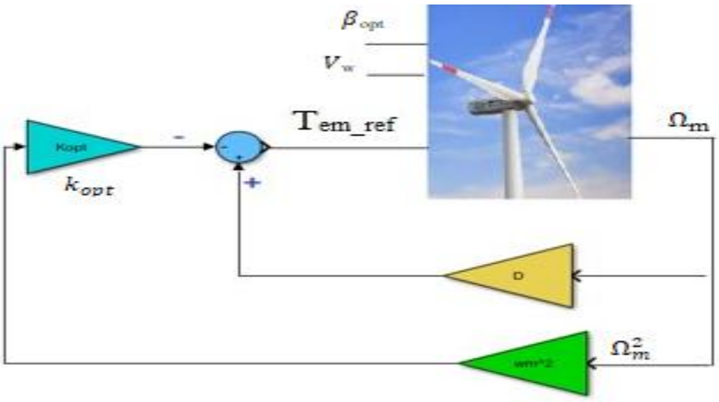

Figure 13. Indirect speed control

5.2 Control structure for switching the crowbar protection

For DFIG-based WECS, several crowbar control techniques have been put forth in recent years [22]. This paper enhances the LVRT capabilities of DFIG-based WECS by applying FLC to the crowbar. Fig 14. displays the FLC that was created in the MATLAB/Simulink environment to operate the Crowbar switch. To find problems, as previously mentioned, the DC bus voltage and rotor current measurements are first compared with reference values. The FLC then receives this error value as an input value. By comparing the FLC results with the DC bus voltage and rotor current, the timing of the crowbar switch is established.

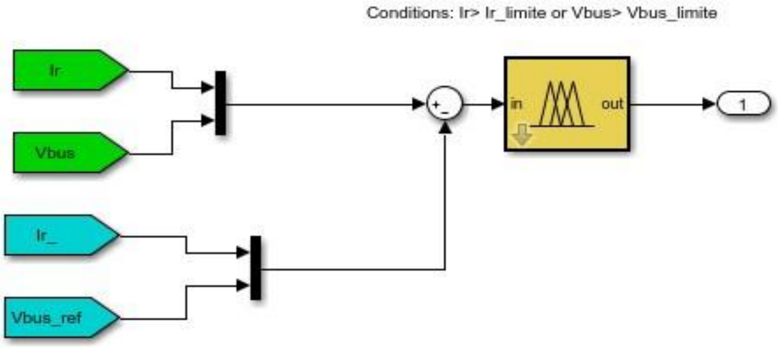

Figure 14. Fuzzy logic controller of crowbar

5.3 The Rotor-Side Control Structure (RSC)

The rotor-side converter vector control scheme with negative sequence compensation with the balanced rotor currents in the event of a voltage dip is shown in Fig 15.

The purpose of RSC is to control the stator and rotor currents to regulate the torque and thus the speed of the wind turbine and obtain maximum energy [43]. The vector control of RSC is based on dq-axis transformation using PI controllers: two controllers are used to control the two d-axis rotor current components (I_{drp}) and (I_{drn}), and two controllers are used to control the two q-axis rotor current components (I_{qrp}) and (I_{qrn}) and speed controller.

Copyright © 2024 by Author/s and Licensed by JISEM. This is an open access article distributed under the Creative Commons Attribution License which permitsunrestricted use, distribution, and reproduction in any medium, provided the original work is properly cited.

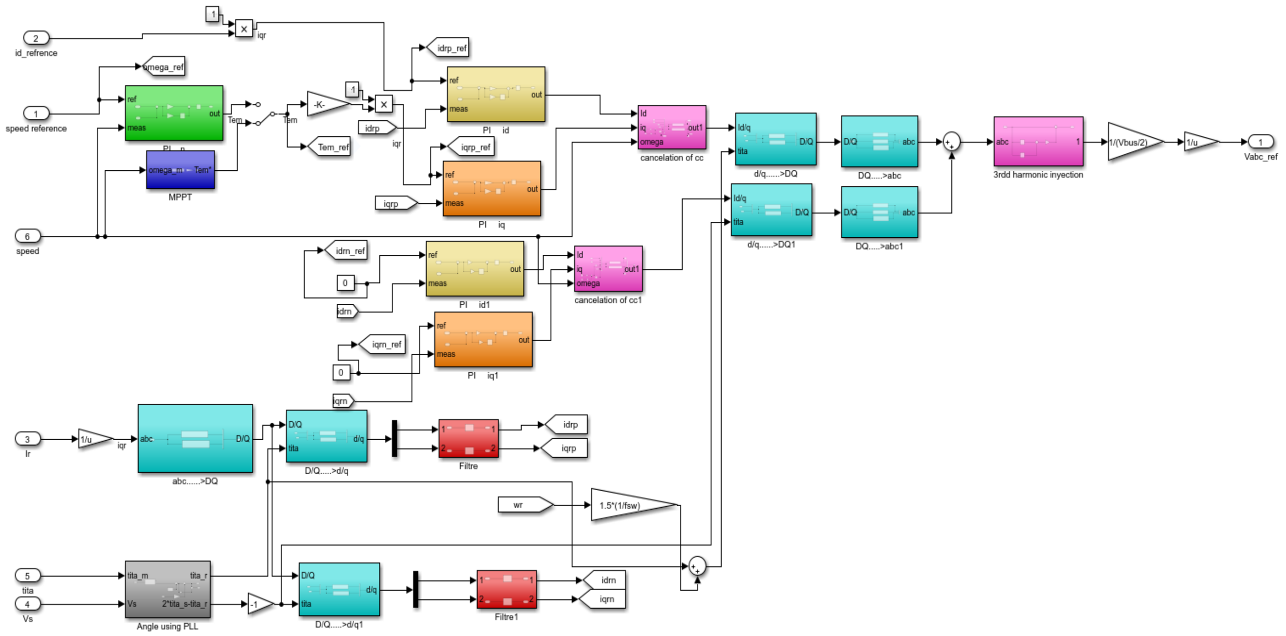

Figure 15. Vector control diagram of the rotor-side converter with compensation of the negative sequence in case of voltage dip.

5.4 The Grid-Side Control Structure (GSC)

Figure 16 shows the control diagram for the grid-side converter with negative sequence compensation with the balanced rotor currents in the event of a voltage dip. In this section, we use the same RSC control strategy, i.e. vector control technique with negative sequence compensation with GSC vector control based on dq-axis transformation using PI controller: two controllers are used to control the two d-axis grid current components (I_{dgp} , I_{dgn}), and two controllers are used to control the two q-axis grid current components using (I_{qgp} , I_{qgn}) and bus continuity controller. The grid voltage angle is determined by the voltage V_s for the PLL used from 3_{Φ} to 2_{Φ} and from 2_{Φ} to 3_{Φ}. To accurately estimate the stator voltage angle, it is highly recommended to use PLL technology, which has a closed-loop control system that guarantees stability and noise suppression of angle estimation. PLL is an excellent method to synchronize a set of three-phase sine wave signals with variable frequency and positive sequence supply voltage [40]. When automatic gain control is enabled, the phase error input of the PLL controller adjusts based on the amplitude of the input signal.

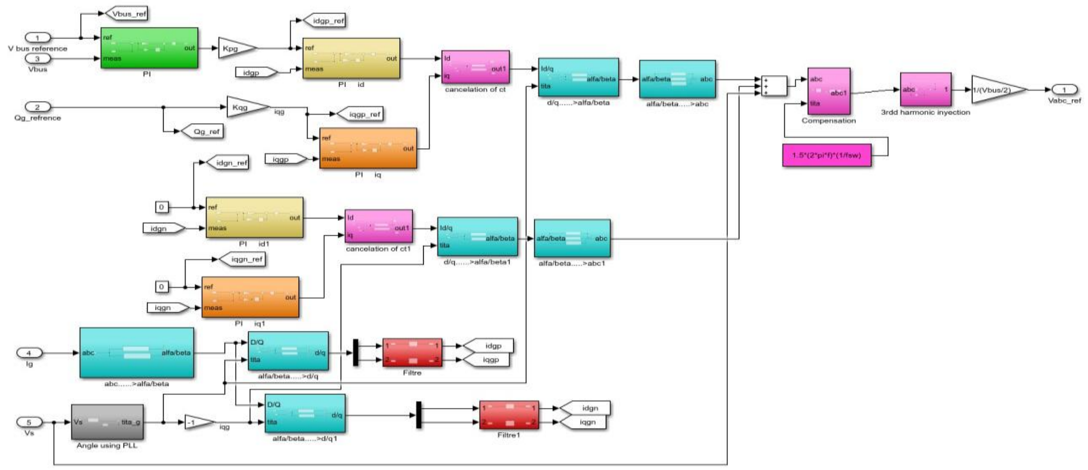

Figure 16. Schematic of the grid side converter control with negative sequence compensation of the stator current in case of voltage dip

Copyright © 2024 by Author/s and Licensed by JISEM. This is an open access article distributed under the Creative Commons Attribution License which permitsunrestricted use, distribution, and reproduction in any medium, provided the original work is properly cited.

Journal of Information Systems Engineering and Management
2025, 10(4)
e-ISSN: 2468-4376
https://www.jisem-journal.com/
Research Article

4. Simulation Results and Discussion

WECS cannot guarantee constant performance during voltage dips, due to converter constraints that limit rotor voltage. In this work, the DFIG-equipped wind turbine is fitted with a crowbar-type protection system that solves the low-voltage problem and guarantees safety without losing control of the whole system, with improved operating conditions using fuzzy logic controller. The flowchart in Fig 17 provides a summary of the developed control technique.

The simulation results show the difference between the voltage dip without crowbar protection and with crowbar protection during the time t=3.15 s to t=4.17 s at a wind speed of 10 m/s.

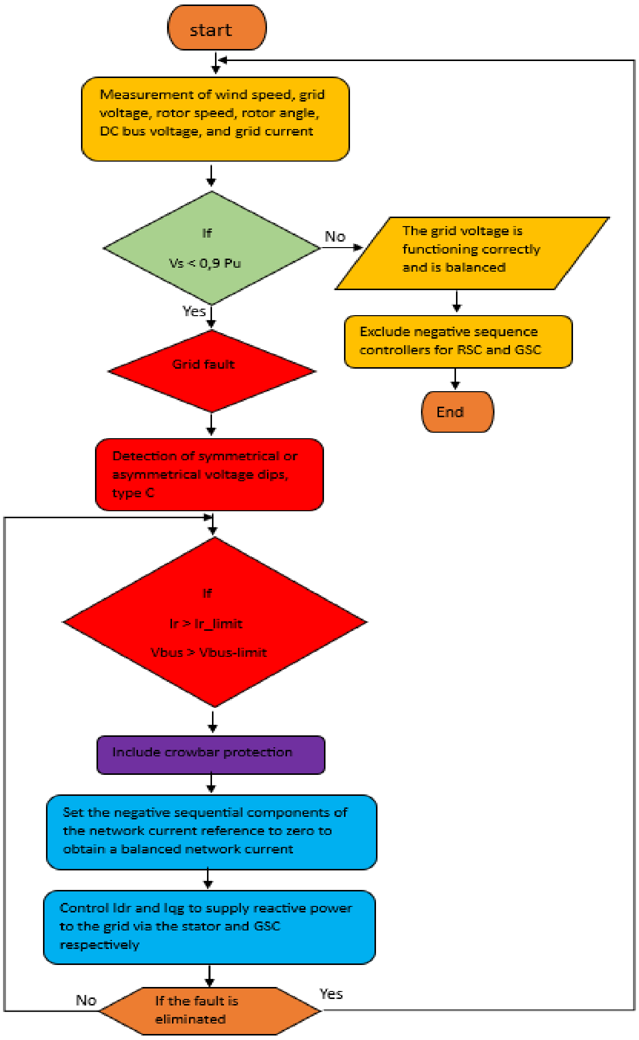

Figure 17. Diagram illustrating the control approach used for both symmetric and asymmetric voltage dips (type C)

6.1 Fault-free system status

This study is carried out using a variable-speed WECS equipped with DFIG. The wind turbine has a rated power of 2.4 MW, while the DFIG has a rated power of 2 MW. The stator voltage is set at 690 V and the frequency at 50 Hz, with a synchronous speed of 1500 rpm. The electrical grid provides three balanced voltages with constant frequency and amplitude during normal operation. According to Eq. (35) the three phases are separated by 120° and have the same voltage values:

$$\begin{cases} V_a = V_{ag}\cos(w_g t + \emptyset) \\ V_b = V_{bg}\cos(w_g t + \emptyset - 120°) \\ V_c = V_{cg}\cos(w_g t + \emptyset - 240°) \end{cases} \quad (35)$$

Copyright © 2024 by Author/s and Licensed by JISEM. This is an open access article distributed under the Creative Commons Attribution License which permitsunrestricted use, distribution, and reproduction in any medium, provided the original work is properly cited.

Figure 18 presents simulation from RSC in fault-free system status: a) Rotor speed; b) Torque; c) Stator voltage; d) Stator current; e) Rotor current.; f) d-axis rotor current for positive and negative sequence; g) q-axis rotor current for positive and negative sequence; h) d-axis rotor voltage for positive and negative sequence; i) q-axis rotor voltage for positive and negative sequence. Figure 18.a shows that in the transient regime, the rotor speed slowly increases and approaches the reference speed until it is superposed on the steady state.

There are some oscillations in the speed, but after a few seconds everything is correct and a short oscillation of the speed is obtained. The strong disturbance we see is caused by the machine starting directly connected to the grid but once this start is rich, we see that the system is controlled correctly. Figure 18.b presents torque and as the load is responsible for the change in torque and since our machine is functioning as a generator, the torque is negative. We can see there is an overshoot during the transient regime due to the connection directly of the machine to the grid and after a few milliseconds, it will decrease to the steady state, and it's clear that torque the electromagnetic torque tracking its reference perfectly.

From Figures 18.c, 18.d and 18. f, the stator and rotor currents produced by the DFIG have a good sinusoidal waveform, and the stator voltage generated by DFIG also has a sine waveform. Figures 18.f et 18.g present respectively d-axis rotor current for positive and negative sequence and q-axis rotor current for positive and negative sequence, (I_{drn} , I_{qrn}) are zero because we used the balanced rotor current method, while (I_{qrp}) is varied as a function of torque and (I_{drp}) is varied as a function of reactive power through stator to the system. Figures 18.h et 18.i present respectively d-axis rotor current for positive and negative sequence and q-axis rotor current for positive and negative sequence, (V_{qrp}) is modified according to (I_{qrp}) and as (I_{drn}, I_{qrn}) are maintained null therefore (V_{drn}, V_{qrn}) has been also zero.

Figure 19 presents simulation from GSC in fault-free system status: a) DC bus voltage; b) Grid current. c) q-axis grid current for positive and negative sequence; d) d-axis grid current for positive and negative sequence; e) d-axis grid voltage for positive and negative sequence; f) q-axis grid voltage for positive and negative sequence; g) Grid reactive power.

From Figure 19.a we see a significant a big overshoot of the DC bus voltage due to the very strong start-up, but after a few seconds the rotor-side converter and the grid-side converter reach their stable operating point and the DC bus voltage decreases towards the reference, the DC bus voltage operates around the reference and reaches the stable state required by the reference. As soon as we have a fairly stable state with oscillation performance on the grid side, we also have very correct operation in the rotor-side converter with its current loops and torque.

From Figure 19.b we can see that the mains voltage takes on a perfectly sinusoidal waveform.

From Figures 19.c and 19.d, the rotor currents along the d-q axis follow their references perfectly, as well as according to Figures 19.f and 19.g, the network voltages follow their references perfectly, and since (I_{dgn}, I_{qgn}) are kept null, we obtain (V_{dgn} , V_{qgn}) null, while the voltage (V_{dgp} ,V_{qgp}) are very small voltages because we have used a feedback voltage from the grid while the grid voltage and current take on a sinusoidal form. In fact, according to grid regulations, reactive power must be zero, and the Figure 18.h confirms this.

Figure 20 presents simulation from fault analysis in fault-free system status: (a) Stator flux, (b) Crowbar current (c) Torque on crowbar.

From Figure 20.b it's clear that no current flows through the crowbar protection, so torque and stator flux are perfect, and Figures 20.a and 20.c confirm this.

Copyright © 2024 by Author/s and Licensed by JISEM. This is an open access article distributed under the Creative Commons Attribution License which permitsunrestricted use, distribution, and reproduction in any medium, provided the original work is properly cited.

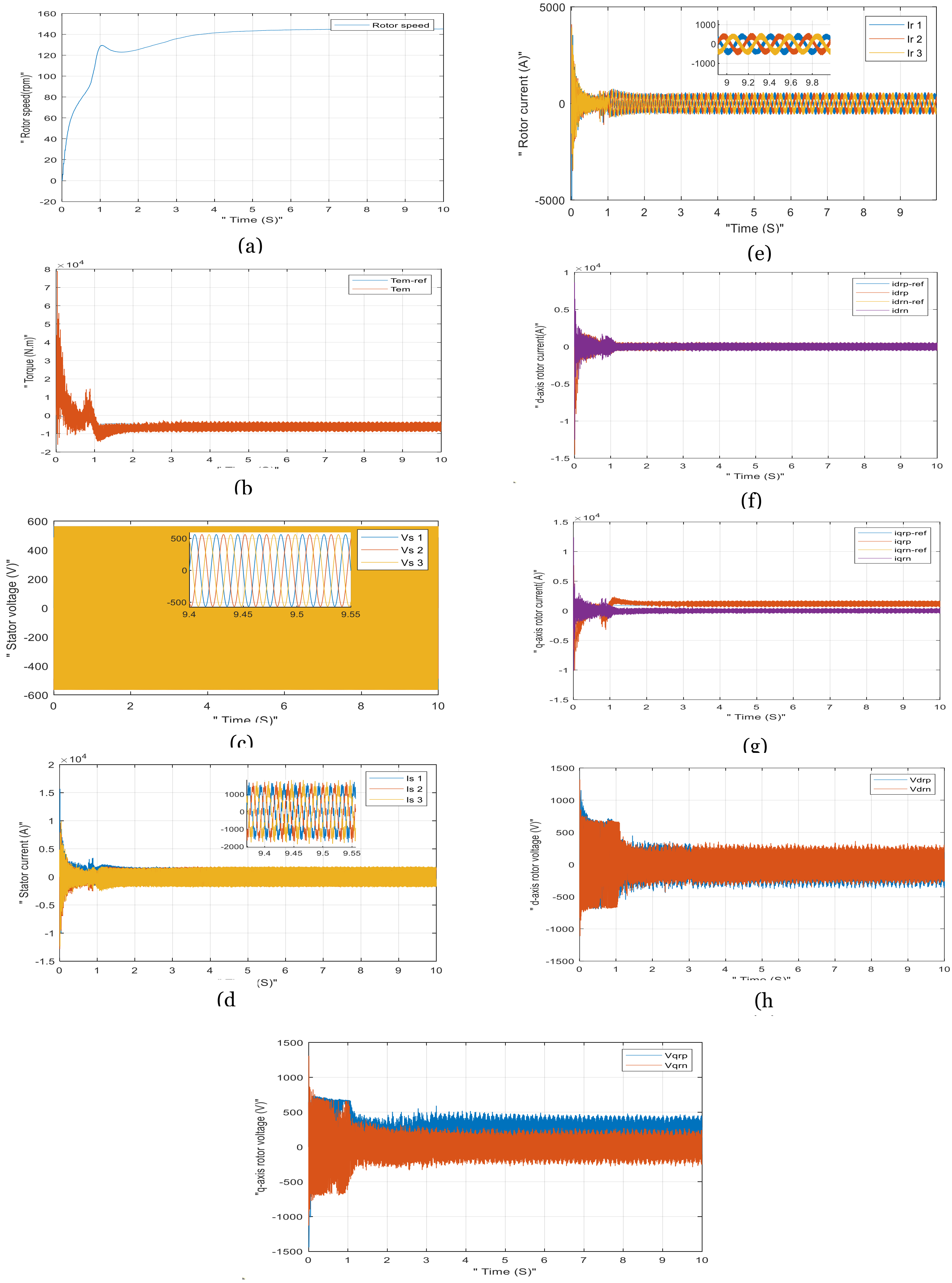

(a) (e)

(b (f)

(c) (g)

(d (h

Figure 18. Results de simula (i) om RSC in fault-free system status

Copyright © 2024 by Author/s and Licensed by JISEM. This is an open access article distributed under the Creative Commons Attribution License which permitsunrestricted use, distribution, and reproduction in any medium, provided the original work is properly cited.

Journal of Information Systems Engineering and Management
2025, 10(4)
e-ISSN: 2468-4376
https://www.jisem-journal.com/

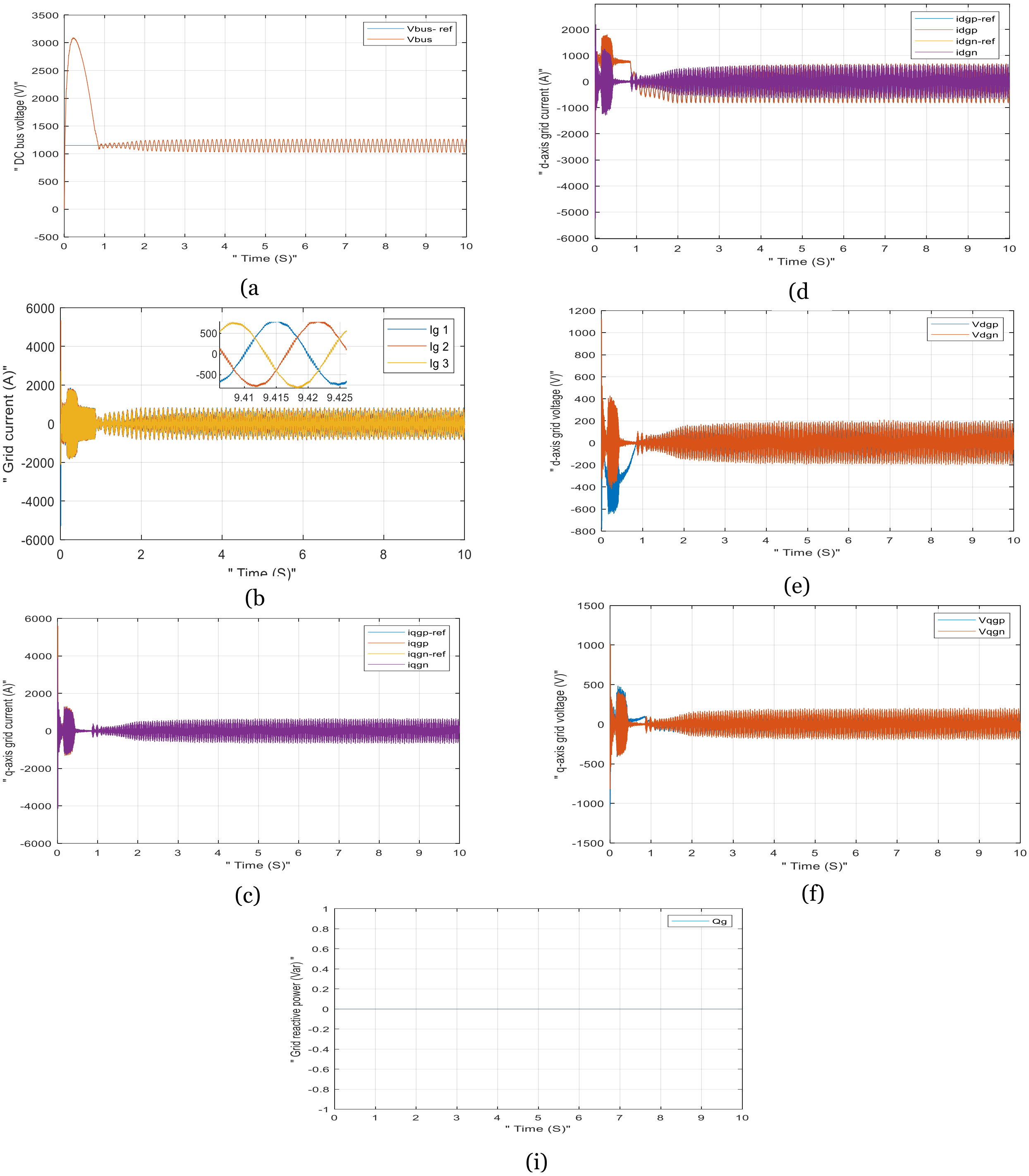

(a

(d

(b

(e)

(c)

(f)

(i)

Figure 19. Results de simulation from GSC during symmetrical voltage dip without crowbar protection

Copyright © 2024 by Author/s and Licensed by JISEM. This is an open access article distributed under the Creative Commons Attribution License which permitsunrestricted use, distribution, and reproduction in any medium, provided the original work is properly cited.

Journal of Information Systems Engineering and Management
2025, 10(4)
e-ISSN: 2468-4376
https://www.jisem-journal.com/

Research Article

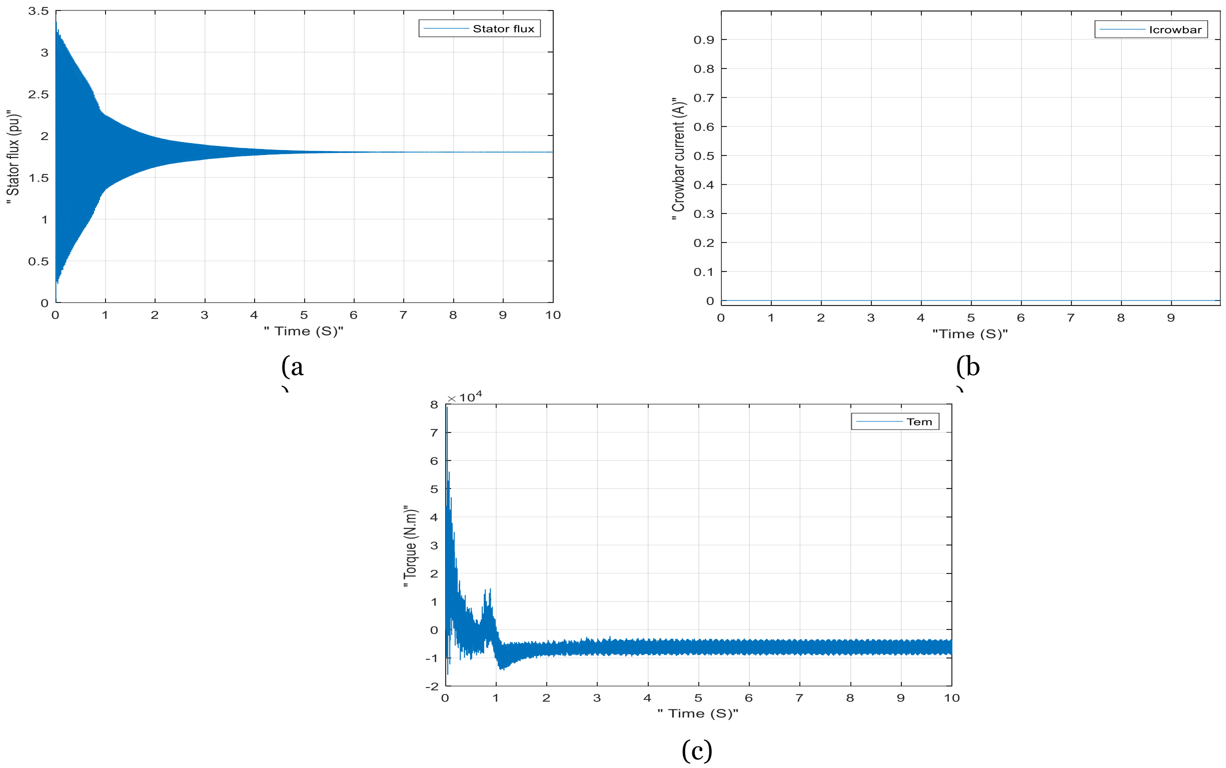

(a)

(b)

(c)

Figure 20. Results de simulation from fault analysis in fault-free system status

6.2 Symmetrical voltage dips without crowbar protection

This part analyzes the DFIG operation with 80 % symmetrical voltage dips, including harmonics without crowbar protection. The DFIG is supposed to operate under normal conditions, at a given instant 3.15 s, a symmetrical voltage dip occurs without FLC protection. DFIG simulation results are examined without the crowbar technique when a balanced three-phase earth fault occurs between the ground and the three phases. During the voltage dip, our examination was conducted on the rotor and grid sides and presented in Figures 21,22. The analysis of faults symmetrical with stator flux is shown in Figure 23. We performed a symmetrical voltage dip from t=3.15 to t=4.17 and we see a notable disturbance in all DFIG parameters. Figure 21.a shows the sudden increase in rotor speed. The (T_{em})figure of the proposed DFIG without FLC at 10 m/s wind speed is shown in Figure 21.b. A symmetrical voltage dip's delay to achieve the reference torque is crucial to the proposed DFIG-based WECS's validity. In this case, the time required is 5s with a severe and strong disturbance. According to from Figure 21.c abrupt change is clear in (V_s) occurred and the voltage present in the grid is only 20% of the nominal voltage, and then the recovery voltage after the time of the voltage dip is produced. As seen from Figure 21.c, The desired (V_s) was obtained by DFIG without FLC in 5 s after the symmetrical voltage dip cleared in 4.17 s. The WECS's recovery time is crucial to the proposed WECS's accuracy and applicability and accuracy of the proposed WECS and as we see in this case the high recovery time. Thus, from the other Figures we see an increase in rotor voltage of the DFIG without FLC $(V_{dr}\ , V_{qr}\ )$ and rotor current of the DFIG without FLC $(I_{dr}\ , I_{qr})$ and stator current of the DFIG without FLC (I_s), which deviate from a sinusoidal waveform, causing a significant torque disturbance during dip. In the GSC, from Figures 22 we observe that the voltage dip without FLC has led to abnormal fluctuations in DC bus voltage and even grid voltage $(V_{dg}\ , V_{qg})$ and current $(I_{qg}\ , I_{dg})$. The suggested system uses 1150 V as its reference Vbus. During the symmetrical voltage dip at 3.15 s, DFIG without FLC becomes unstable until 4.17 s. On the other hand, the DFIG without FLC does not reach the reference Vbus until the drop period ends at time 4.6s. The DFIG without FLC does not reach the reference (V_{bus})any faster. Figure 22.a shows the presence of a strong DC bus disturbance from time 3.1s to 4.17s, clearly indicating that the signal does not follow its reference during the dip period without FLC. So, from Figures 22.b and 22.c we can see that the rotor voltages of the DFIG without FLC were disturbed during the dip period. Figures 22.e and 22.f also show

Copyright © 2024 by Author/s and Licensed by JISEM. This is an open access article distributed under the Creative Commons Attribution License which permitsunrestricted use, distribution, and reproduction in any medium, provided the original work is properly cited.

excessive fluctuations in grid currents along the d-q axis, but despite the strong disturbance presented we see from figure 22.d that the grid current remains balanced and takes on a perfectly sinusoidal waveform thanks to the GSC negative sequence control. Reactive power generally has a value of zero, and when there is a voltage dip, a reference for reactive power is produced based on the current during the voltage dip, as shown in Figure 22.i. The presence of the produced reactive power value is an expected value because in practice, as required by grid regulations, we should supply a substantial amount of reactive current, which can also be achieved by the GSC supplying negative reactive power (Q_g) during the voltage dip. The I_{qg} controls the reactive power of the GSC, and for balanced network currents, I_{qg} should be set to zero. Figure 23.b shows fault current detection through the crowbar protection, and this leads to a sudden disturbance in torque and a reduction in the stator magnetic field stator flux, which is confirmed by Figures 23.a and 23.c.

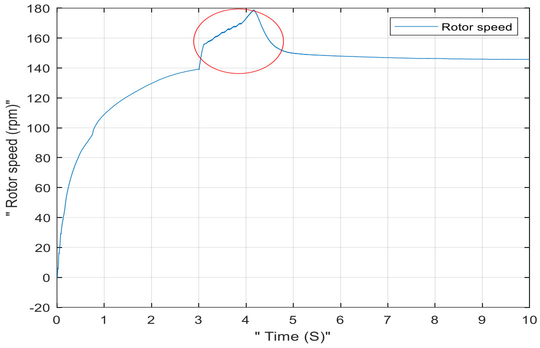

(a
)

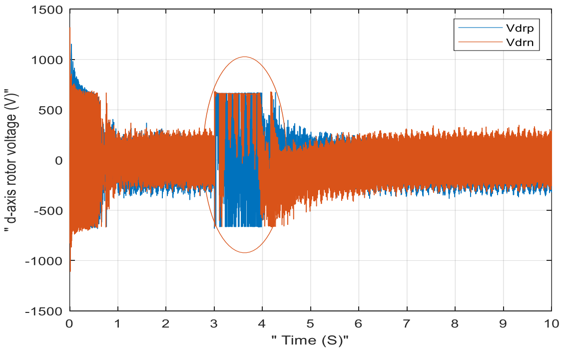

(e)

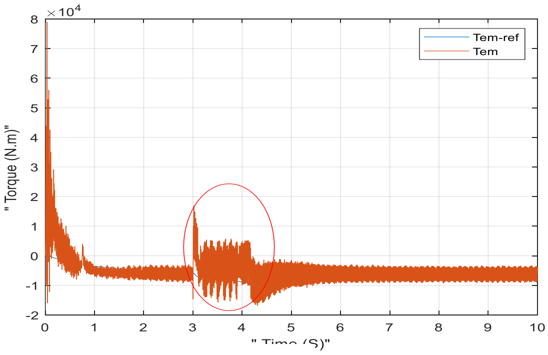

(b
)

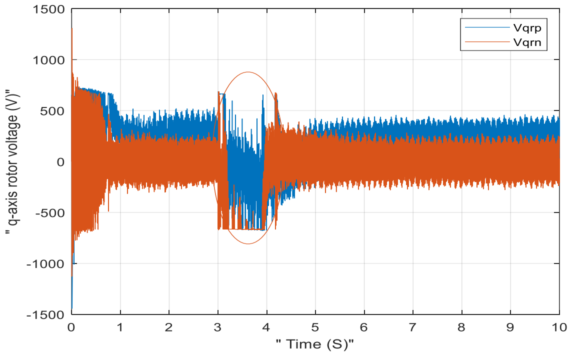

(f)

Copyright © 2024 by Author/s and Licensed by JISEM. This is an open access article distributed under the Creative Commons Attribution License which permitsunrestricted use, distribution, and reproduction in any medium, provided the original work is properly cited.

Journal of Information Systems Engineering and Management
2025, 10(4)
e-ISSN: 2468-4376
https://www.jisem-journal.com/

Research Article

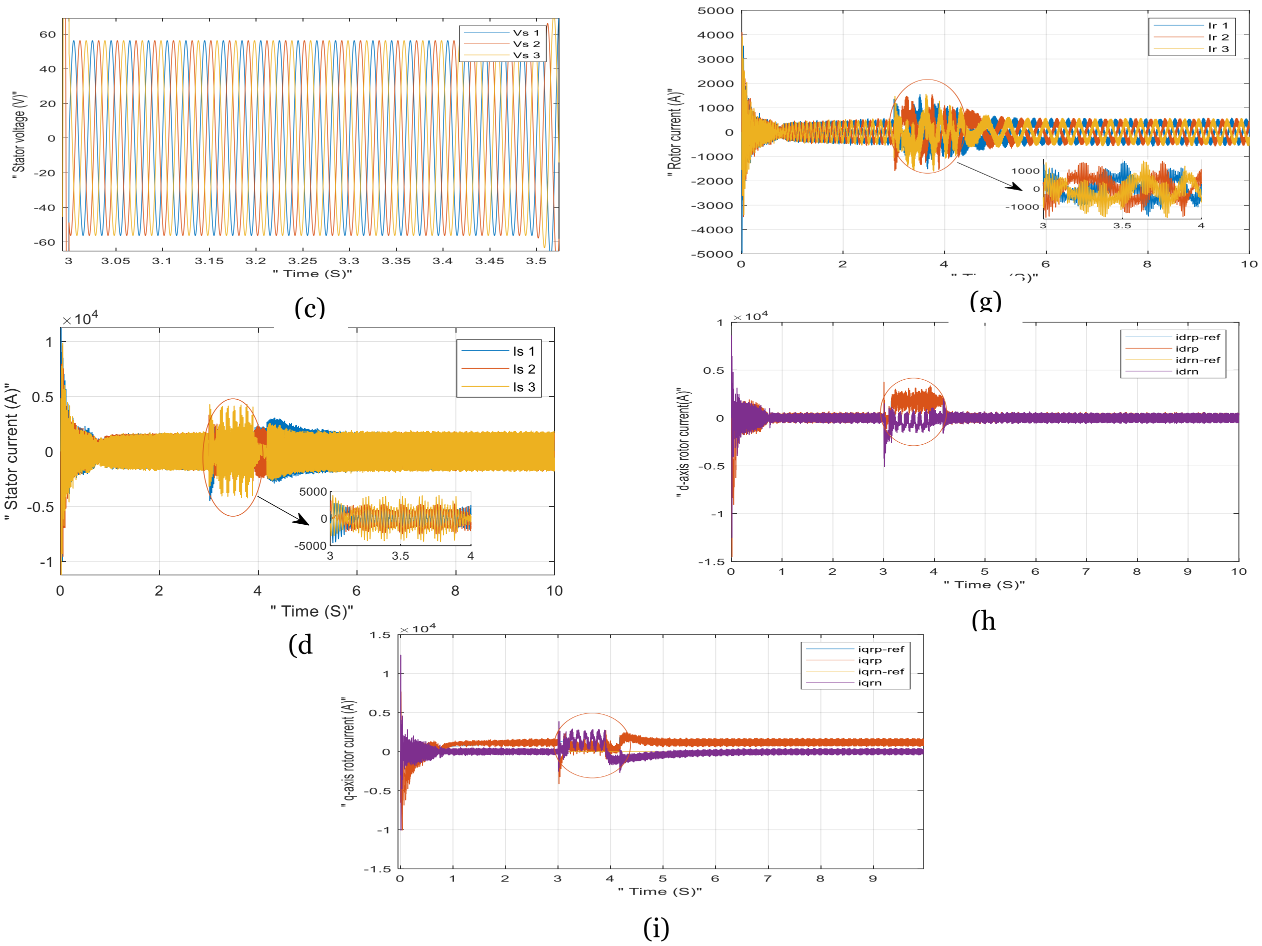

(c)

(g)

(d

(h

(i)

Figure 21. Results de simulation from RSC during symmetrical voltage dip without crowbar protection

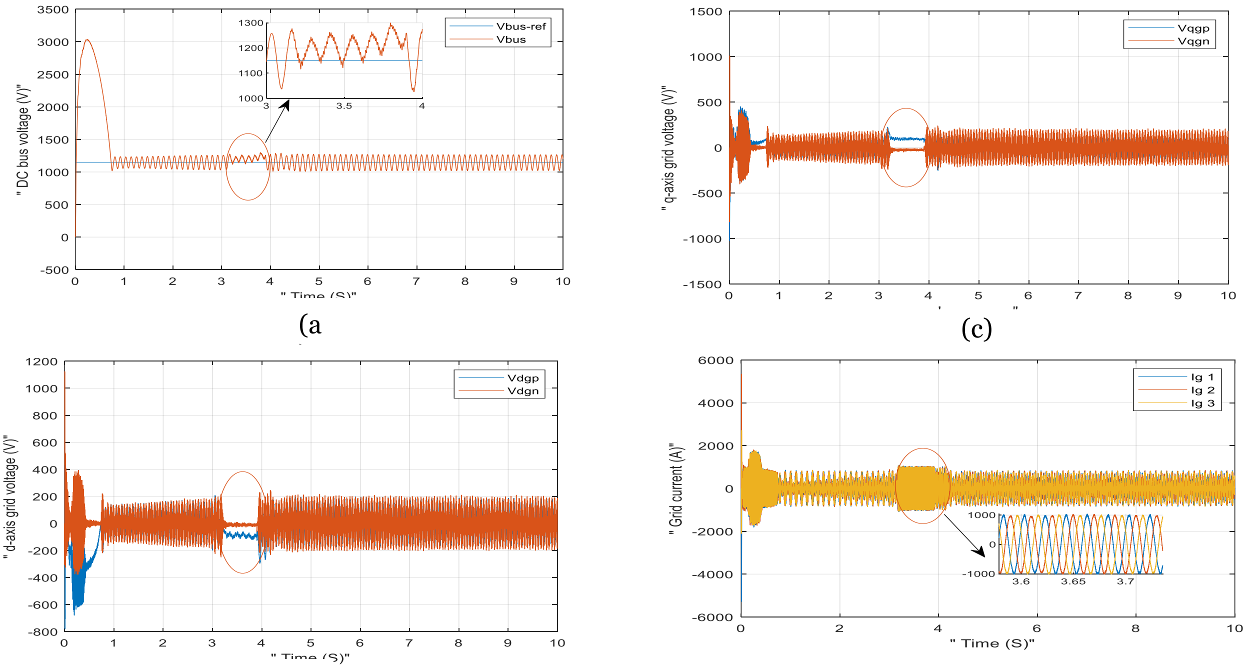

(a

(c)

(b

(d

Copyright © 2024 by Author/s and Licensed by JISEM. This is an open access article distributed under the Creative Commons Attribution License which permitsunrestricted use, distribution, and reproduction in any medium, provided the original work is properly cited.

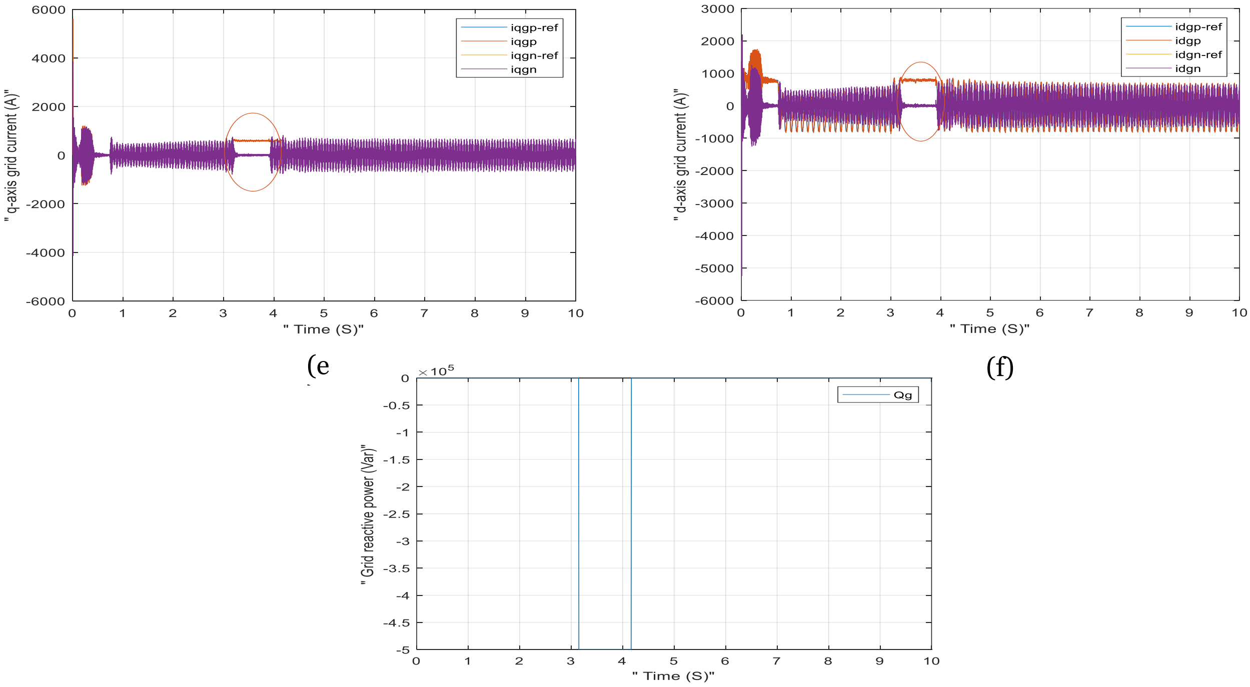

(e

(f)

(i)

Figure 22. Results de simulation from GSC during symmetrical voltage dip without crowbar protection

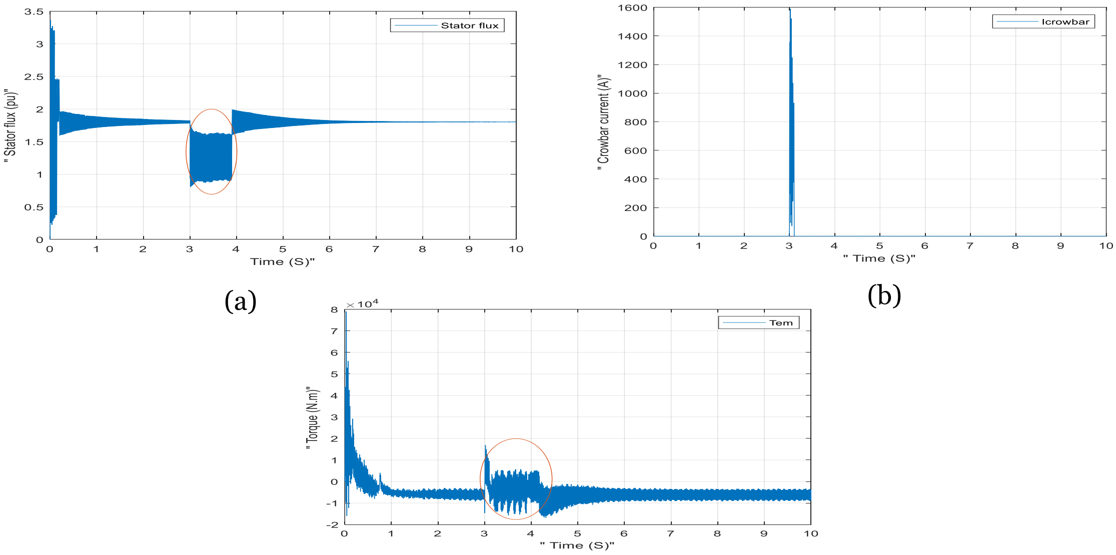

(a)

(b)

(c)

Figure 23. Results de simulation from fault analysis during symmetrical voltage dip without crowbar protection a)

6.3 Asymmetrical voltage dips without crowbar protection

There are many types of unbalanced voltage dips. In this study, we have highlighted the asymmetrical phase-to-phase type C fault in the grid. Therefore, it is important to monitor the 2-Φ asymmetrical disturbance during network disturbances. In the same system, DFIG simulation results are observed without crowbar protection during an asymmetrical 2-Φ fault between one phase and one phase. In this part, rotor current references are the sum of positive

Copyright © 2024 by Author/s and Licensed by JISEM. This is an open access article distributed under the Creative Commons Attribution License which permitsunrestricted use, distribution, and reproduction in any medium, provided the original work is properly cited.

and negative sequences. we'll need to generate positive-order and negative-order voltages and currents using the DFIG, and we'll need to introduce negative-order currents to ensure precise control of the generator. To ensure that each sequence is effectively regulated, it is essential to handle each sequence independently. During voltage dip, our examination was carried out on the rotor and grid side and presented the same Figures as the symmetry examination. Figures 24-25 show the results on the generator and grid sides respectively while Figure 26 shows the results of the fault analysis. We have caused a voltage dip in the grid in which the DFIG voltages have dropped unbalanced, there is a voltage a that remains stable but voltages b and c have dropped. The dip occurs from t=3.15s to t=4.17s, causing asymmetry and unbalance in the grid, and leading to a significant disturbance in the stator which is detected by the RSC and then by the GSC.

At t=3.15 s, we see a strong disturbance in all DFIG parameters, as shown in Figure 24.c we can see the asymmetrical disturbance in stator voltage during the voltage dip, so we can't get full control, and from the Figures below. Recovery time following an asymmetric voltage dip is important for ensuring the intended DFIG-based WECS is valid. We see in this case that following a 2-Φ asymmetrical voltage dip, the system maintained its rated voltage when the fault resolved in 4.17 s. We also observe a strong disturbance in stator current (I_s), rotor voltage in positive and negative sequence (V_{dr} ,V_{qr}) and rotor current in positive and negative sequence (I_{qr} ,I_{dr}), and the torque. Eventually, however, the voltage recovers, signifying the end of the disturbance for the system and enabling it to operate with acceptable performance. Torque oscillations are mainly due to the I_{qr+} imbalance, which is responsible for torque regulation. The DFIG electromagnetic torque figure shows that the system's (T_{em}) overshoot is significantly elevated in the absence of FLC. In 4.17 s, the T_{em} of the DFIG without FLC reached reference (T_{em}) following the clearing of the asymmetric voltage dip. According Figure 24.d, 24.e, 24.h and 24.i the results show that a voltage dip is accompanied by an increase in (I_s ,I_r) and (V_{dr} ,V_{qr}), causing a reduction in stator flux and grid voltage. Figure 24.e shows that the rotor current does not assume a sinusoidal form during the voltage dip, (I_r) at the beginning we have the sub-synchronous mode because we are inferior to the synchronous speed than at the point where the reference speed is equal to the synchronous speed, the currents are not sinusoidal at this point of functioning they become DC current, the machine functions like a synchronous motor, finally we have the sub-synchronous mode we obtain the sequences (abc). According to Figure 24.f, 24.g it is clear that the rotor currents along the d-q axis are very disturbed and are not following their references. Convertor analysis from the grid side we can see disturbances in the system parameters and a total loss of control .Figure 24.c, 24.d, 24.e, 24.f show a trajectory deviation in (V_{dgp} , V_{dgn} , V_{qgp} , V_{qgn} , I_{dgn} , I_{qgn} , I_{qgn} I_{qgp}). We need to add a negative current control to the positive current loops to resolve this asymmetry in the grid and be in control of the generator. At the beginning of the dip, Figure.25. a shows DC bus voltage oscillations are visible and the bus is not able to control this enormous overvoltage due to the rotor power flowing through the rotor, so there is a very large overshoot and the I_{dg+} tries to bring the bus voltage close to the reference. The suggested system's reference V_{bus} voltage is 1150 V. The DFIG without FLC does not catch the reference Vbus voltage and is stabilized in 1.5 s. The Vbus overshoot of the DFIG without FLC is very high. At 3.15s we have the sudden positive reactive current demand given by I_{qg+} when the negative I_{dg-} and I_{qg-} components are held equal to zero. The grid voltage V_s is asymmetrical but the grid current I_g is balanced with good operation and this is due to the negative sequence I_{dg-} and I_{qg-} that we have added to the GSC but as the DC bus voltage remains disturbed and does not follow its reference so the presence of the protection mechanism is essential. Figure 26.b shows fault current detection through the crowbar protection, and this leads to a sudden disturbance in torque and a reduction in the stator magnetic field stator flux, which is confirmed by Figures 26.a and 26.c.

Copyright © 2024 by Author/s and Licensed by JISEM. This is an open access article distributed under the Creative Commons Attribution License which permitsunrestricted use, distribution, and reproduction in any medium, provided the original work is properly cited.

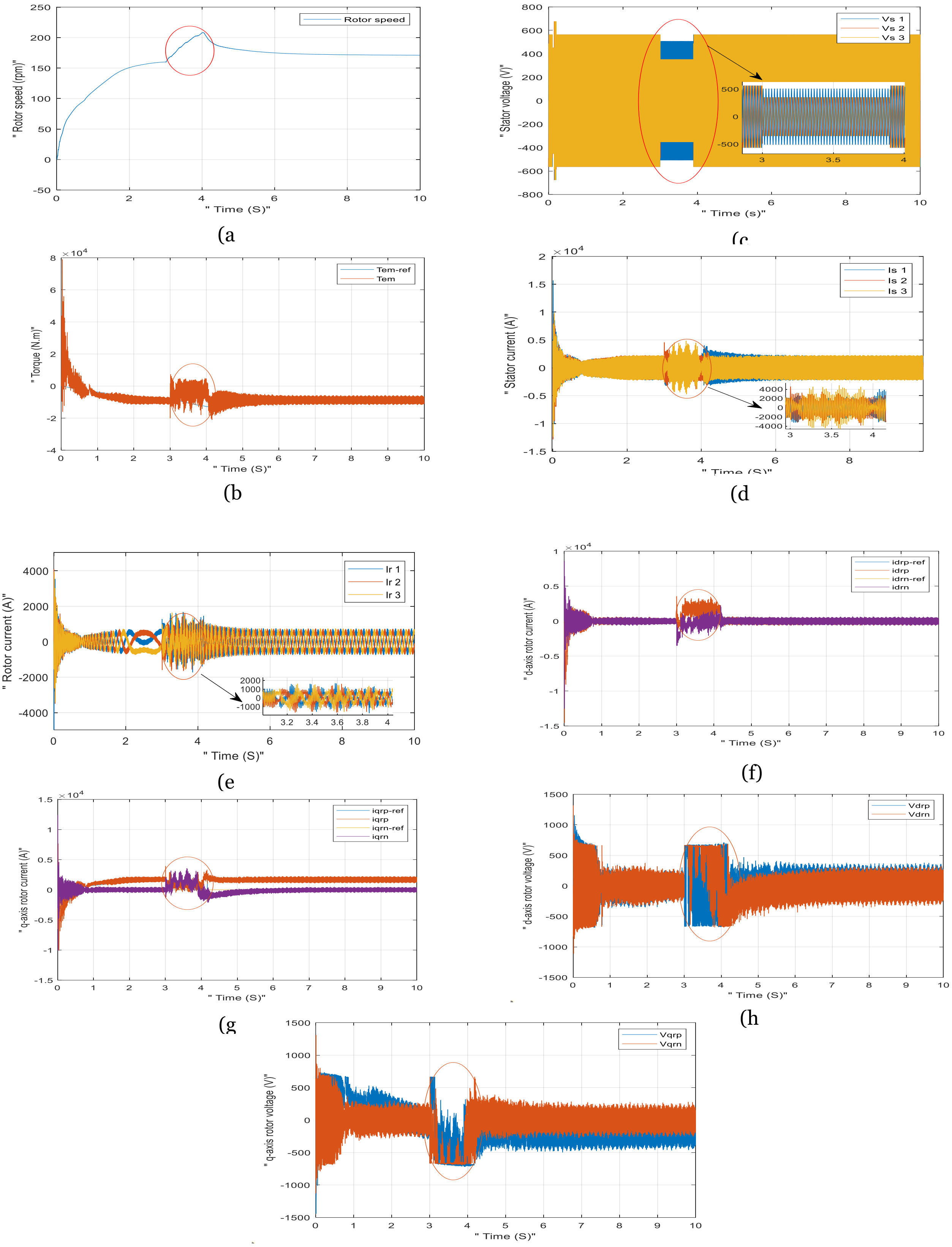

(a

(c

(b

(d

(e

(f)

(g

(h

(i)

Figure 24. Results de simulation from RSC during asymmetrical voltage dip without crowbar protection

Copyright © 2024 by Author/s and Licensed by JISEM. This is an open access article distributed under the Creative Commons Attribution License which permitsunrestricted use, distribution, and reproduction in any medium, provided the original work is properly cited.

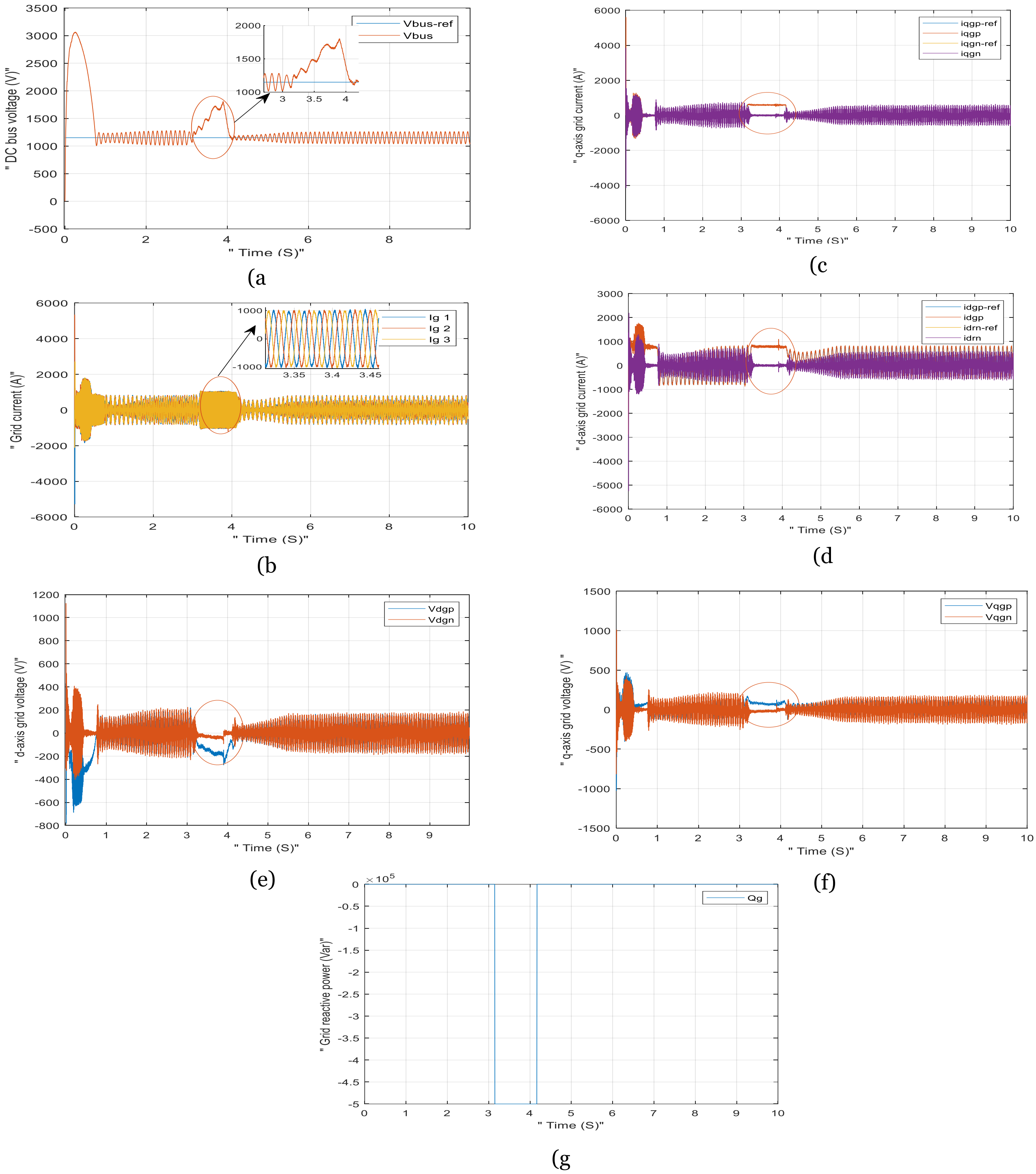

(a

(c

(b

(d

(e)

(f)

(g

Figure 25. Results de simulation from GSC during asymmetrical voltage dip without crowbar protection

Copyright © 2024 by Author/s and Licensed by JISEM. This is an open access article distributed under the Creative Commons Attribution License which permitsunrestricted use, distribution, and reproduction in any medium, provided the original work is properly cited.

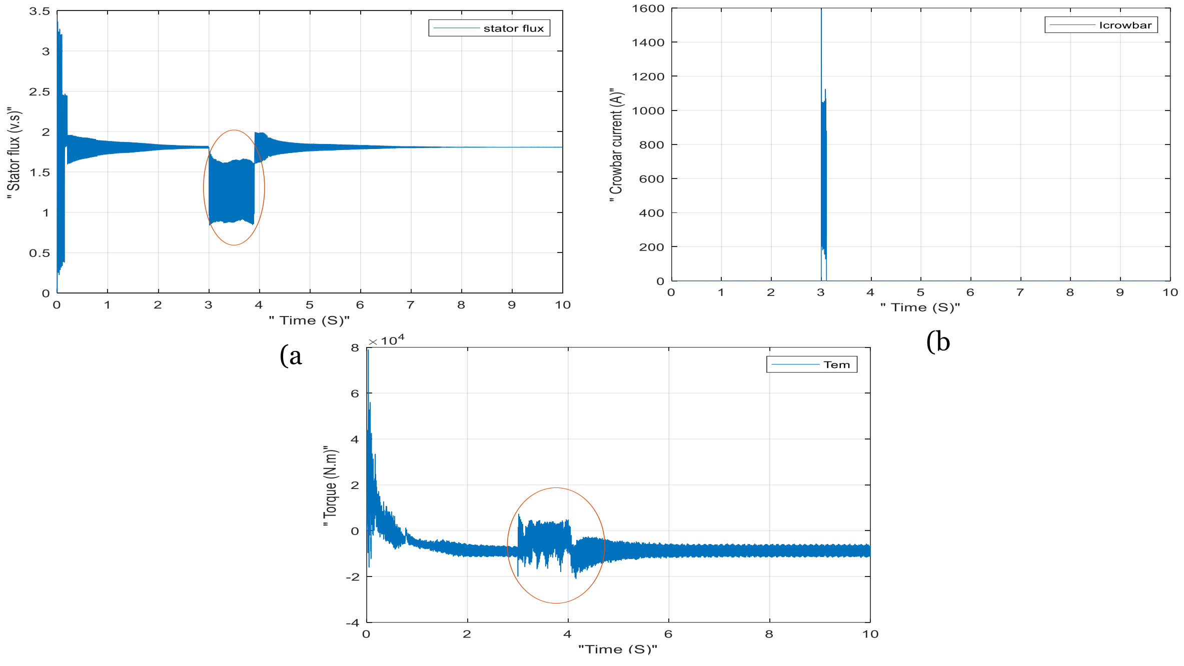

(a

(b

(c)

Figure 26. Results de simulation from fault analysis during asymmetrical voltage dip without crowbar protection

6.4 Asymmetrical voltage dips with crowbar protection

This part analyzes the DFIG operation with asymmetrical type-C voltage dips, with crowbar protection. The DFIG is supposed to operate under normal conditions, at a given instant 3.15 s, a voltage dip occurs. DFIG simulation results are examined with the crowbar protection controlled by the fuzzy logic. During voltage dip, our examination was carried out on the rotor and grid side and presented and presented in Figure 27-28 respectively.As programmed, as soon as the sudden voltage dip occurs, the crowbar protection is activated, causing all current and energy to flow through the protection resistor as, as shown in the fault analysis in Figure 29 During this activation, we observe that all rotor current flows through the protection circuit, thus protecting the RSC. Moreover, activation is expressed as a percentage, indicating that stator currents are high and that there is a significant torque peak.

From Figure 27 we can see that the presence of disturbance is much reduced compared to the fault without crowbar protection. From Figure 27.b, 27.d and 27.e we see that all parameters $(I_s\,, I_r\,, T_{em})$ are disturbed just once in the 1 instant of the fault. The electromagnetic torque of the DFIG with FLC at a wind speed of 10 m/s is expressed in Figure 27.b. For the suggested DFIG-based WECS to be valid, it is crucial to determine how long it takes to reach the reference torque following an asymmetric voltage dip. According to Figure 27.b (T_{em}) reaches its reference faster and without overshooting compared to the system without FLC, which was relatively high. According to the test findings, the suggested DFIG with FLC is also reliable and valid in terms of (T_{em}) .

The WECS's recovery time is crucial to the proposed WECS's accuracy and applicability. From Figure 27.c we see DFIG with FLC reached the desired (V_s) in 4.4 s, while from Figure 24.c DFIG without FLC reached the desired (V_s) in 5 s. The suggested DFIG-based WECS provides acceptable and realistic outcomes. WECS without FLC recovered more slowly than DFIG with FLC. From the standpoint of (V_s), DFIG with FLC produced more accurate findings.

From Figure. 27.f and 27.g we can see that during activation of the protection the disturbance of the rotor current along the d-q axis is greatly reduced, as is a small disturbance in the rotor voltage, as shown in Figure. 27.h and 27.i. When the protection circuit is activated, we can observe from Figure 28.a, that the DC bus voltage differs from both the symmetrical and asymmetrical cases without crowbar protection. In this part, the DC bus continues to operate around its reference value even during the voltage dip, thanks to our protection circuit as shown in Figure 28.a. The suggested system's reference V_{bus} is 1150 V.

Copyright © 2024 by Author/s and Licensed by JISEM. This is an open access article distributed under the Creative Commons Attribution License which permitsunrestricted use, distribution, and reproduction in any medium, provided the original work is properly cited.

The DFIG with FLC arrived at the reference Vbus faster compared to those without FLC. We see that Vbus follows perfectly its reference during voltage dips asymmetrical with FLC. The DC bus voltage fluctuation without FLC is larger than the Vbus voltage fluctuation with FLC, as seen in Figures 28.a and 24.a. The Vbus overshoot with FLC is smaller than V_{bus} the without FLC following the asymmetrical voltage dip. According to the simulation results, during asymmetrical voltage dip, DFIG with FLC is more practical from the perspective of (V_{bus}).

From Figure 28, it is clear that the (V_{dgp} ,V_{qgp} ,I_{dgp},I_{qgp}) remain functional around the reference even during the asymmetric fall, thanks to the activation of the crowbar protection controlled by the fuzzy logic. Moreover, from de Figure 28.g we can see that the reactive power remains at zero during the voltage dip, as if our system were faultless.

Figure 29.b shows the detection of the fault current by the crowbar protection, but according to Figures 29.a, 29.c we see a very slight disturbance of the torque and a small reduction of the stator magnetic field flux. Our aim with this protection is to ensure that the system remains controllable even during voltage dips and to eliminate the need for reactive power.

The rotor windings, capacitors, and converters were protected from overcurrent during the voltage dip by the Crowbar. Thanks to FLC, the suggested method yields more valid and appropriate findings when compared to the DFIG without FLC. The suggested crowbar technique shows a respectable improvement in the failure behavior of the system under consideration, thanks to simulation findings and behavior analysis.

Copyright © 2024 by Author/s and Licensed by JISEM. This is an open access article distributed under the Creative Commons Attribution License which permitsunrestricted use, distribution, and reproduction in any medium, provided the original work is properly cited.

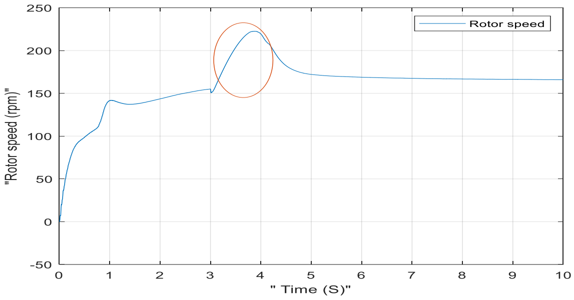

(a

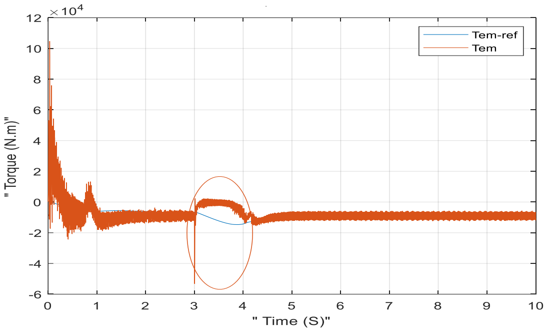

(b

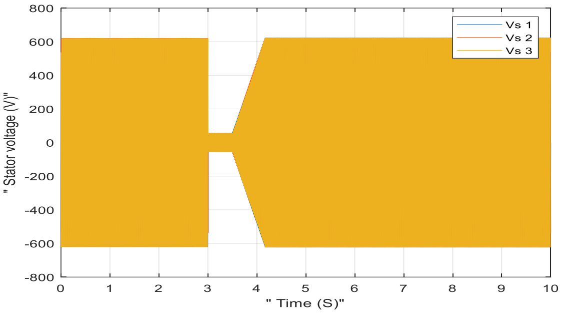

(c)

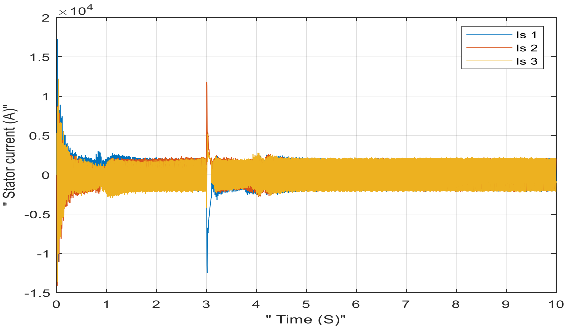

(d

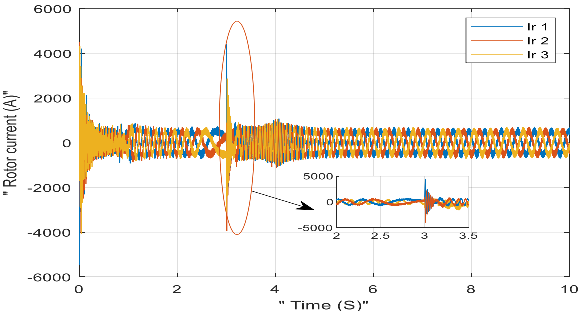

(e)

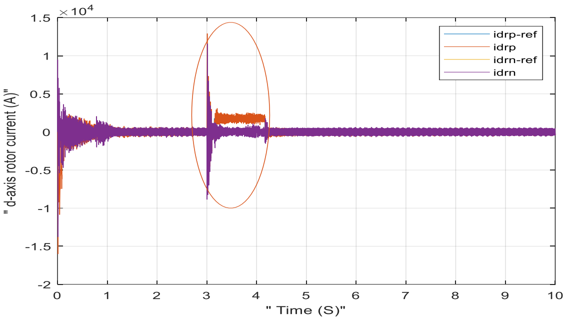

(f)

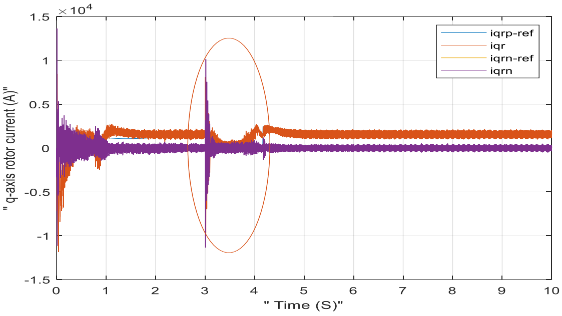

(g

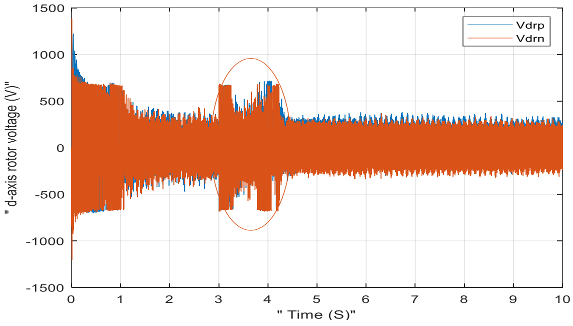

(h

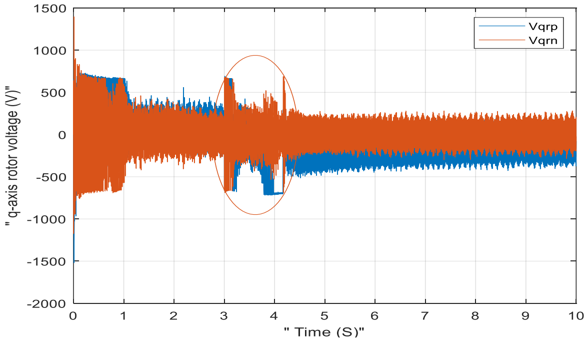

(i)

Copyright © 2024 by Author/s and Licensed by JISEM. This is an open access article distributed under the Creative Commons Attribution License which permitsunrestricted use, distribution, and reproduction in any medium, provided the original work is properly cited.

Figure 27. Results de simulation from RSC during asymmetrical voltage dip with crowbar protection

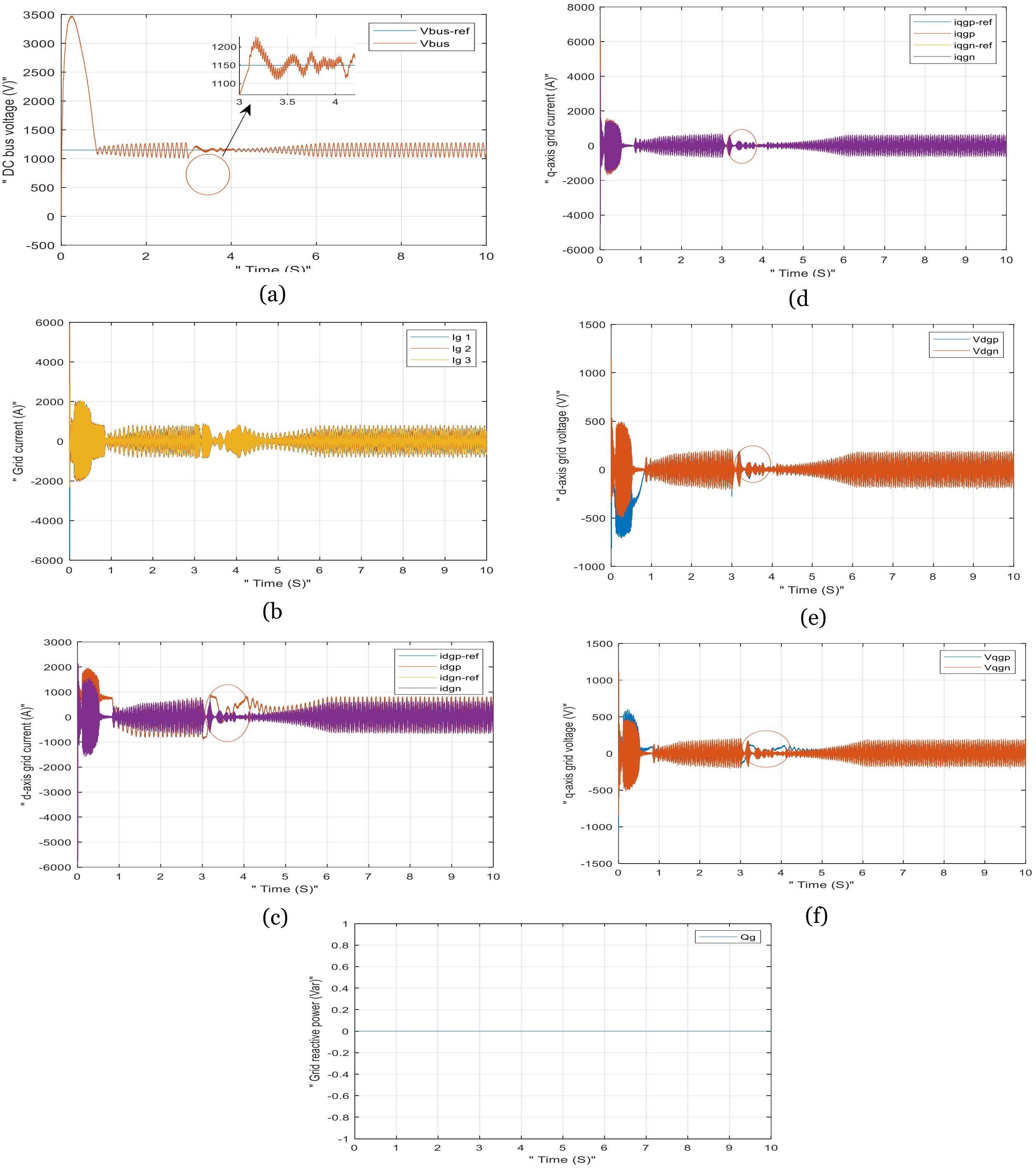

(a) (d

(b (e)

(c) (f)

(g

Figure 28. Results de simulation from GSC during asymmetrical voltage dip with crowbar protection

Copyright © 2024 by Author/s and Licensed by JISEM. This is an open access article distributed under the Creative Commons Attribution License which permitsunrestricted use, distribution, and reproduction in any medium, provided the original work is properly cited.

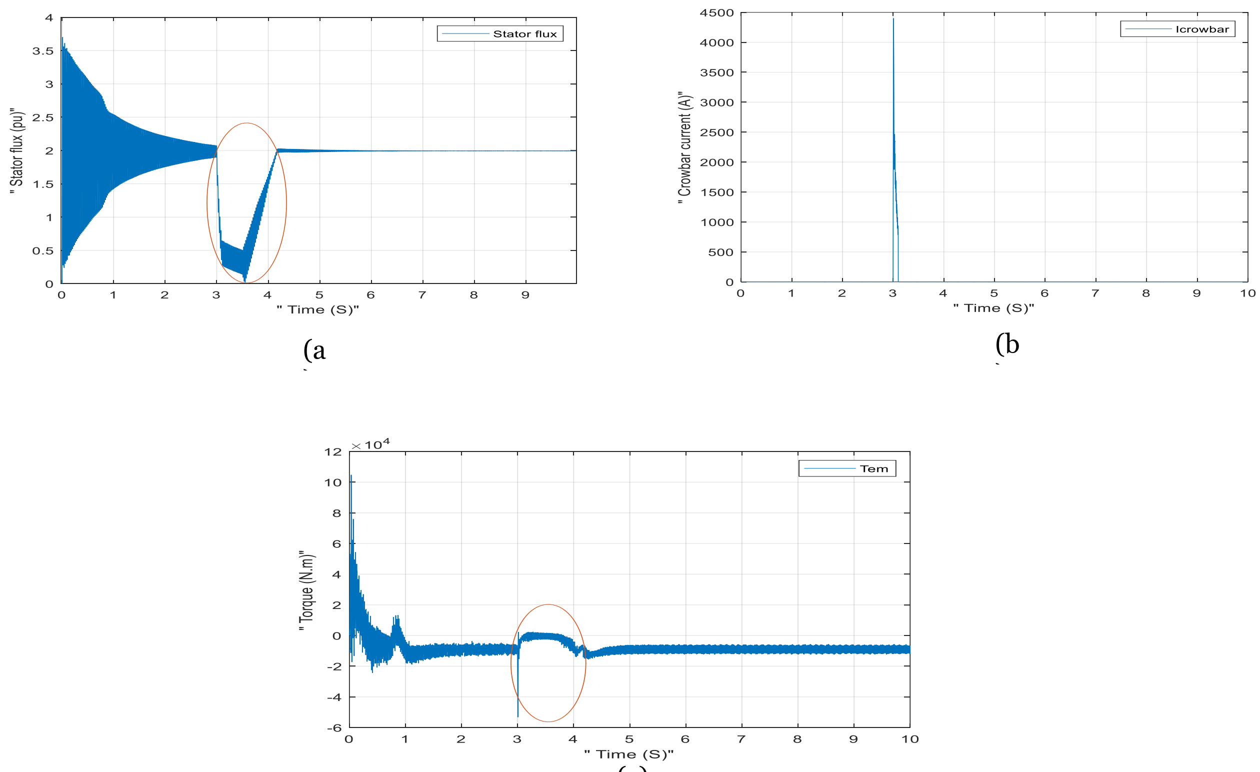

(a

(b

(c)

Figure. 29. Results de simulation from fault analysis during asymmetrical voltage dip with crowbar protection

CONCLUSION

In this study, low voltage ride-through is achieved under symmetric and asymmetric Type-C voltage dip by improving DFIG-based WECS. In order to guarantee LVRT functionality during a voltage dip, the DFIG must stay linked to the grid in accordance with grid standards. The suggested WECS with reactive power support is intended to be more consistent, dependable, and applicable to the FLC-based crowbar protection circuit. Model and simulate it with Matlab/Simulink using real DFIG parameters. To control RSC and GSC, we use negative sequence vector control based on dq axis transformation. The suggested DFIG-based WECS was examined under both symmetric and asymmetric voltage sag conditions with a constant wind speed of 10 m/s. The results verified in Matlab/Simulink show that the symmetric/asymmetric voltage sag capability of the proposed WECS improves fault continuity. The results of the simulation confirm that the suggested WECS with FLC-based crowbar-protected DFIG is reliable, applicable, and feasible.

REFERENCES

[1] Global Wind Energy Council. [Online]. Available: https://www. gwec.net/. Accessed 15 Feb 2021

[2] Chhipą, A. A., Vyas, S., Kumar, V., & Joshi, R. R. (2022). MPPT optimisation techniques and power electronics for renewable energy systems : wind and solar energy systems. *International Journal Of Swarm Intelligence*, *7*(2), 141. https://doi.org/10.1504/ijsi.2022.123092.

[3] Prasad, R. M., & Mulla, M. A. (2020). Mathematical Modeling and Position-Sensorless Algorithm for Stator-Side Field-Oriented Control of Rotor-Tied DFIG in Rotor Flux Reference Frame. *IEEE Transactions On Energy Conversion*, *35*(2), 631-639. https://doi.org/10.1109/tec.2019.2956255.

[4] Rajendran, M., & Kumar, L. A. (2020). Modeling and Simulation of a DFIG-Based Wind Energy System. Dans *Lecture notes in electrical engineering* (p. 31-49). https://doi.org/10.1007/978-981-15-7245-6_4.

[5] Cho, H. H., Strezov, V., & Evans, T. (2023). A review on global warming potential, challenges and opportunities of renewable hydrogen production technologies. *Sustainable Materials And Technologies*, *35*, e00567. https://doi.org/10.1016/j.susmat.2023.e00567.

Copyright © 2024 by Author/s and Licensed by JISEM. This is an open access article distributed under the Creative Commons Attribution License which permitsunrestricted use, distribution, and reproduction in any medium, provided the original work is properly cited.

[6] Hassan, Q., Abdulateef, A. M., Hafedh, S. A., Al-Samari, A., Abdulateef, J., Sameen, A. Z., Salman, H. M., Al-Jiboory, A. K., Wieteska, S., & Jaszczu, M. (2023). Renewable energy-to-green hydrogen : A review of main resources routes, processes and evaluation. *International Journal Of Hydrogen Energy*, *48*(46), 17383-17408. https://doi.org/10.1016/j.ijhydene.2023.01.175.

[7] Chakraborty, N., Choudhury, N. B. D., & Tiwari, P. (2023). Profit Maximization of Retailers with Intermittent Renewable Sources and Energy Storage Systems in Deregulated Electricity Market with Modern Optimization Techniques : A Review. *Renewable Energy Focus*, *47*, 100492. https://doi.org/10.1016/j.ref.2023.100492.

[8] Afghoul, H., Krim, F., Babes, B., Beddar, A., & Kihel, A. (2018). Design and real time implementation of sliding mode supervised fractional controller for wind energy conversion system under sever working conditions. *Energy Conversion And Management*, *167*, 91-101. https://doi.org/10.1016/j.enconman.2018.04.097.

[9] Guediri, A., Hettiri, M., & Guediri, A. (2023). Modeling of a Wind Power System Using the Genetic Algorithm Based on a Doubly Fed Induction Generator for the Supply of Power to the Electrical Grid. *Processes*, *11*(3), 952. https://doi.org/10.3390/pr11030952.

[10] Chhipą, A. A., Vyas, S., Kumar, V., & Joshi, R. R. (2020). Role of Power Electronics and Optimization Techniques in Renewable Energy Systems. Dans *Algorithms for intelligent systems* (p. 167-175). https://doi.org/10.1007/978-981-15-8045-1_17.

[11] Global Wind Energy Council. Global Wind Report 2022. Available online: https://gwec.net/ (accessed on 9 May 2022).

[12] Kadi, S., Imarazene, K., Berkouk, E. M., Benbouhenni, H., & Abdelkarim, E. (2022). A direct vector control based on modified SMC theory to control the double-powered induction generator-based variable-speed contra-rotating wind turbine systems. *Energy Reports*, *8*, 15057-15066. https://doi.org/10.1016/j.egyr.2022.11.052.

[13] Chen, H., El-Refaie, A., Zuo, Y., Cai, S., Tang, J., Liu, Y., & Lee, C. (2023). Design and Analysis of a Variable-Speed Constant-Amplitude Wind Generator for Stand-Alone DC Power Applications. *IEEE Transactions On Industrial Electronics*, *70*(8), 7731-7742. https://doi.org/10.1109/tie.2023.3234149.

[14] Long, Y., Chen, Y., Xu, C., Li, Z., Liu, Y., & Wang, H. (2023). The role of global installed wind energy in mitigating CO2 emission and temperature rising. *Journal Of Cleaner Production*, *423*, 138778. https://doi.org/10.1016/j.jclepro.2023.138778.

[15] González, G. N., De Angelo, C. H., & Aligia, D. A. (2022). A control strategy for DFIG-based systems operating under unbalanced grid voltage conditions. *International Journal Of Electrical Power & Energy Systems*, *142*, 108273. https://doi.org/10.1016/j.ijepes.2022.108273.

[16] Kong, X., Wang, X., Abdelbaky, M. A., Liu, X., & Lee, K. Y. (2022). Nonlinear MPC for DFIG-based wind power generation under unbalanced grid conditions. *International Journal Of Electrical Power & Energy Systems*, *134*, 107416. https://doi.org/10.1016/j.ijepes.2021.107416.

[17] Draft Report on Indian Wind Grid Code, [Online].Available: https://niwe.res.in/NIWE_OLD/Hindi/Docu/Wind_grid_code_ for_India%20.pdf Accessed 2 Feb 2019.

[18] Chang, Y., Hu, J., Tang, W., & Song, G. (2018). Fault Current Analysis of Type-3 WTs Considering Sequential Switching of Internal Control and Protection Circuits in Multi Time Scales During LVRT. *IEEE Transactions On Power Systems*, *33*(6), 6894-6903. https://doi.org/10.1109/tpwrs.2018.2844206.

[19] Muisyo, I. N., Muriithi, C. M., & Kamau, S. I. (2022). Enhancing low voltage ride through capability of grid connected DFIG based WECS using WCA-PSO tuned STATCOM controller. *Heliyon*, *8*(8), e09999. https://doi.org/10.1016/j.heliyon.2022.e09999.

[20] Chakraborty, A., & Maity, T. (2023). Integrated control algorithm for fast and accurate detection of the voltage sag with low voltage ride-through (LVRT) enhancement for doubly-fed induction generator (DFIG) based wind turbines. *Control Engineering Practice*, *131*, 105393. https://doi.org/10.1016/j.conengprac.2022.105393.

[21] Firouzi, M., & Gharehpetian, G. B. (2018). LVRT Performance Enhancement of DFIG-Based Wind Farms by Capacitive Bridge-Type Fault Current Limiter. *IEEE Transactions On Sustainable Energy*, *9*(3), 1118-1125. https://doi.org/10.1109/tste.2017.2771321.

Copyright © 2024 by Author/s and Licensed by JISEM. This is an open access article distributed under the Creative Commons Attribution License which permitsunrestricted use, distribution, and reproduction in any medium, provided the original work is properly cited.

[22] Xiao, F., Yongjun, X., Zhang, K., Zhang, Z., & Yin, X. (2023). Fault characteristics analysis of DFIGWT in whole LVRT process considering control strategy switching between RSC and Crowbar. *International Journal Of Electrical Power & Energy Systems*, *145*, 108615. https://doi.org/10.1016/j.ijepes.2022.108615.

[23] Tohidi, S., & Mohammadi-Ivatloo, B. (2016). A comprehensive review of low voltage ride through of doubly fed induction wind generators. *Renewable & Sustainable Energy Reviews*, *57*, 412-419. https://doi.org/10.1016/j.rser.2015.12.155.

[24] Noureldeen, O., & Hamdan, I. (2018). A novel controllable crowbar based on fault type protection technique for DFIG wind energy conversion system using adaptive neuro-fuzzy inference system. *Protection And Control Of Modern Power Systems*, *3*(1). https://doi.org/10.1186/s41601-018-0106-0.

[25] Liu, R., Ye, J., Wang, X., Sun, P., Pei, J., & Hu, J. (2020). Dynamic Stability Analysis and Improved LVRT Schemes of DFIG-Based Wind Turbines During a Symmetrical Fault in a Weak Grid. *IEEE Transactions On Power Electronics*, *35*(1), 303-318. https://doi.org/10.1109/tpel.2019.2911346.

[26] Döşoğlu, M. K. (2020). Crowbar hardware design enhancement for fault ride through capability in doubly fed induction generator-based wind turbines. *ISA Transactions*, *104*, 321-328. https://doi.org/10.1016/j.isatra.2020.05.024.

[27] Liu, X., Li, X., & Jiao, D. (2019c). Theoretical Study on Control Strategy of Grid-Connected High Voltage Ride Through in Doubly-Fed Wind Farm. *IEEE Access*, *7*, 107453-107464. https://doi.org/10.1109/access.2019.2933695.

[28] Arduini, F. R., Asada, E. N., & Bellmunt, O. G. (2021). Comparison between a crowbar and an R-SFCL to improve Fault Ride-Through Capacity of DFIG-based Wind Turbines. *IEEE Madrid PowerTech*. https://doi.org/10.1109/powertech46648.2021.9494924.

[29] Gencer, A. (2022). FRT Capability Enhancement of Wind Turbine Based on DFIG Using Machine Learning. *Niğde Ömer Halisdemir Üniversitesi Mühendislik Bilimleri Dergisi*. https://doi.org/10.28948/ngumuh.1165004.

[30] Hu, J., Huang, Y., Wang, D., Yuan, H., & Yuan, X. (2015). Modeling of Grid-Connected DFIG-Based Wind Turbines for DC-Link Voltage Stability Analysis. *IEEE Transactions On Sustainable Energy*, *6*(4), 1325-1336. https://doi.org/10.1109/tste.2015.2432062.

[31] Morshed, M. J., & Fekih, A. (2018). A Fault-Tolerant Control Paradigm for Microgrid-Connected Wind Energy Systems. *IEEE Systems Journal*, *12*(1), 360-372. https://doi.org/10.1109/jsyst.2016.2531718.

[32] Döşoğlu, M. K. (2020b). Crowbar hardware design enhancement for fault ride through capability in doubly fed induction generator-based wind turbines. *ISA Transactions*, *104*, 321-328. https://doi.org/10.1016/j.isatra.2020.05.024.

[33] Yu, L. (2016). The fault ride through technologies for doubly fed induction generator wind turbines. *Wind Engineering*, *40*(1), 31-49. https://doi.org/10.1177/0309524x15624342.

[34] López, J., Gubía, E., Sanchis, P., Roboam, X., & Marroyo, L. (2008). Wind Turbines Based on Doubly Fed Induction Generator Under Asymmetrical Voltage Dips. *IEEE Transactions On Energy Conversion*, *23*(1), 321-330. https://doi.org/10.1109/tec.2007.914317.

[35] Thomas, T., Prince, A., Kumar, P., & Cheriyan, E. P. (2022). Real-time hardware emulation of WECS based on DFIG during unbalanced type-B and type-E voltage dips for enhanced low voltage ride-through. *Electrical Engineering*, *104*(5), 3717-3732. https://doi.org/10.1007/s00202-022-015776.

[36] Bekiroğlu, E., & Yazar, M. D. (2023). Fault-Ride through Improvement of DFIG under Symmetrical/Asymmetrical Voltage Dips. *Electric Power Components And Systems*, *51*(5), 510-523. https://doi.org/10.1080/15325008.2023.2179135.

[37] Benbouhenni, H., Bizon, N., Mosaad, M. I., Çolak, İ., Djilali, A., & Benbouhenni, H. (2024). Enhancement of the power quality of DFIG-based dual-rotor wind turbine systems using fractional order fuzzy controller. *Expert Systems With Applications*, *238*, 121695. https://doi.org/10.1016/j.eswa.2023.121695.

[38] Villanueva, I., Rosales, A., Ponce, P., & Molina, A. (2018). Grid-Voltage-Oriented Sliding Mode Control for DFIG Under Balanced and Unbalanced Grid Faults. *IEEE Transactions On Sustainable Energy*, *9*(3), 1090-1098. https://doi.org/10.1109/tste.2017.2769062.

Copyright © 2024 by Author/s and Licensed by JISEM. This is an open access article distributed under the Creative Commons Attribution License which permitsunrestricted use, distribution, and reproduction in any medium, provided the original work is properly cited.

[39] Din, Z., Zhang, J., Zhu, Y., Zheng, X., & El-Naggar, A. (2019). Impact of Grid Impedance on LVRT Performance of DFIG System With Rotor Crowbar Technology. *IEEE Access*, *7*, 127999-128008. https://doi.org/10.1109/access.2019.2938207.

[40] Shekhar, A., Ramirez-Elizondo, L., Feng, X., Kontos, E., & Bauer, P. (2017). Reconfigurable DC Links for Restructuring Existing Medium Voltage AC Distribution Grids. *Electric Power Components And Systems*, *45*(16), 1739-1746. https://doi.org/10.1080/15325008.2017.1346005.

[41] Nair, R., & Narayanan, G. (2020). Stator Flux Based Model Reference Adaptive Observers for Sensorless Vector Control and Direct Voltage Control of Doubly-Fed Induction Generator. *IEEE Transactions On Industry Applications*, 1. https://doi.org/10.1109/tia.2020.2988426.

[42] Li, C., Cao, Y., Li, B., Liu, B., Feng, Q., & Chen, P. (2023). A novel low voltage ride-through scheme for DFIG based on the cooperation of hybrid energy storage system and crowbar circuit. *Journal Of Energy Storage*, *73*, 108879. https://doi.org/10.1016/j.est.2023.108879.

[43] [43] Xiao, X., Yang, R. H., Chen, X., Zheng, Z., & Li, C. (2017). Enhancing fault ride-through capability of DFIG with modified SMES-FCL and RSC control. *Iet Generation Transmission & Distribution*, *12*(1), 258-266. https://doi.org/10.1049/iet-gtd.2016.2136.

Copyright © 2024 by Author/s and Licensed by JISEM. This is an open access article distributed under the Creative Commons Attribution License which permitsunrestricted use, distribution, and reproduction in any medium, provided the original work is properly cited.